1-2017

Multispectrum Analysis of the Oxygen A-band

Brian J. Drouin

D. Chris Benner

Linda R. Brown

... .

V. Malathy Devi
William & Mary, mdvenk@wm.edu

See next page for additional authors

Recommended Citation

Drouin, Brian J.; Benner, D. Chris; Brown, Linda R.; ., ...; Devi, V. Malathy; and al., et, Multispectrum Analysis of the Oxygen A-band (2017). *Journal of Quantitative Spectroscopy and Radiative Transfer*, 186, 118-138. https://doi.org/10.1016/j.jqsrt.2016.03.037

Author Manuscript

Accepted for publication in a peer-reviewed journal

NIST National Institute of Standards and Technology • U.S. Department of Commerce

Published in final edited form as:

J Quant Spectrosc Radiat Transf. 2017 January ; 186: 118–138. doi:10.1016/j.jqsrt.2016.03.037.

Multispectrum analysis of the oxygen A-band

Brian J. Drouin[a], **D. Chris Benner**[b], **Linda R. Brown**[a], **Matthew J. Cich**[a], **Timothy J. Crawford**[a], **V. Malathy Devi**[b], **Alexander Guillaume**[a], **Joseph T. Hodges**[c], **Eli J. Mlawer**[d], **David J. Robichaud**[e], **Fabiano Oyafuso**[a], **Vivienne H. Payne**[a], **Keeyoon Sung**[a], **Edward H. Wishnow**[f], and **Shanshan Yu**[a]

[a]Jet Propulsion Laboratory - NASA, California Institute of Technology, 4800, Oak Grove Drive, Pasadena, CA 91109-8099, USA

[b]Department of Physics, College of William and Mary, Williamsburg, VA, USA

[c]Material Measurement Laboratory, National Institute of Standards and Technology, 100 Bureau Drive, Gaithersburg, Maryland 20899, USA

[d]Atmospheric and Environmental Research, Lexington, MA, USA

[e]National Renewable Energy Laboratory, 15013 Denver West Parkway, Golden, Colorado 80401, USA

[f]University of California Berkeley, Department of Physics and Space Sciences Laboratory, Berkeley, CA 94720, USA

Abstract

Retrievals of atmospheric composition from near-infrared measurements require measurements of airmass to better than the desired precision of the composition. The oxygen bands are obvious choices to quantify airmass since the mixing ratio of oxygen is fixed over the full range of atmospheric conditions. The OCO-2 mission is currently retrieving carbon dioxide concentration using the oxygen A-band for airmass normalization. The 0.25% accuracy desired for the carbon dioxide concentration has pushed the required state-of-the-art for oxygen spectroscopy. To measure O_2 A-band cross-sections with such accuracy through the full range of atmospheric pressure requires a sophisticated line-shape model (Rautian or Speed-Dependent Voigt) with line mixing (LM) and collision induced absorption (CIA). Models of each of these phenomena exist, however, this work presents an integrated self-consistent model developed to ensure the best accuracy.

It is also important to consider multiple sources of spectroscopic data for such a study in order to improve the dynamic range of the model and to minimize effects of instrumentation and associated systematic errors. The techniques of Fourier Transform Spectroscopy (FTS) and Cavity Ring-Down Spectroscopy (CRDS) allow complimentary information for such an analysis. We utilize multispectrum fitting software to generate a comprehensive new database with improved accuracy based on these datasets. The extensive information will be made available as a multi-dimensional

PACS: 33.70.-w, 33.70.Fd, 33.70.Jg, 33.15.-e, 33.15.Mt, 33.20.Ea

cross-section (ABSCO) table and the parameterization will be offered for inclusion in the HITRANonline database.

Keywords

oxygen; atmospheric absorption; collision-induced absorption; multispectrum fitting; spectral lineshapes

2. Introduction

The quantification of Earth's carbon cycle is essential to a fundamental understanding of Earth's climate. The concentration of carbon dioxide varies temporally and geographically based on the variety of sources and sinks operating in the eco-system, atmosphere, cryo-sphere and oceans. The OCO-2 mission was built and designed as a precision tool for the inference of surface fluxes at the parts per million (ppm or μmol/mol) scale across the globe. The method chosen for global atmospheric measurements utilizes reflected and scattered solar radiation in the near infrared (0.7–2.2 μm), which is absorbed by oxygen and carbon dioxide in amounts proportional to the airmass and carbon dioxide concentration, respectively. This light is gathered on orbit, dispersed in a grating spectrometer, and detected at three band-wide intervals, two for carbon dioxide and one for oxygen. These measurements, in concert, enable determination of carbon dioxide concentration along the ray paths through the atmosphere. Due to the relatively high abundance of carbon dioxide (> 400 ppm) the desired 1 ppm accuracy requires high signal to noise (SNR) measurements combined with a high fidelity retrieval of information from the acquired spectra.

Early in the mission development, atmospheric databases [1, 2, 3] were evaluated and found to lack accurate lineshape information at the level required by the OCO/OCO-2 missions [4]. Initial development of the Atmospheric CO_2 Observations from Space (ACOS) algorithm [5, 6, 7, 8], relegated spectroscopic information into the multi-dimensional ABSorption COefficient (ABSCO) table that is accessed at runtime so that complex lineshape routines would not be recomputed for millions of retrievals. Improvements to the ACOS algorithm and the ABSCO table [9] were fostered by generation of new laboratory data and truth testing with the Greenhouse Gases Observing SATellite (GOSAT) [10] and the Total Carbon Column Observing Network (TCCON)[11] datasets. Since launch, major advances have been made in the spectroscopy of the relevant spectral regions that aim to reduce remaining retrieval biases and persistent systematic features in the retrieval residuals.

Focused efforts to improve the oxygen A-band database using Fourier Transform [12, 13] and Cavity Ring Down Spectroscopy (CRDS) were published in the years leading up to launch including (1) precise and accurate position measurements for multiple isotopologues [12, 14, 15] (2) precise and accurate intensity measurements [12, 14, 16, 17, 18, 19, 20] (3) lineshape narrowing determinations for air and self collisional interactions [12, 13, 14, 17] (4) estimates for the temperature dependence of the broadening parameters [21] (5) determinations of line-mixing (LM) and collision-induced absorption (CIA) for high pressures [22], as well as atmospheric pressures in the P-branch [23] and (6) estimates of the extent of water broadening [24, 25, 26, 27]. Much of this information was absorbed into the

most recent update of HITRAN [28], with the exceptions for the self-shift coefficient [14] and partial LM/CIA information [23]. Additionally, the OCO-2 retrieval algorithm uses the full A-band (P and R branches) and so there has remained a need for information beyond these P-branch-only CRDS investigations.

Small but persistent biases between the remotely sensed airmass and validation measurements [29], especially at long paths near atmospheric pressure, necessitated further reconciliation. Considering the known interdependences between line-mixing and collision-induced absorption at high pressures [30], this multispectrum analysis effort was pushed forward in an attempt to critically evaluate the datasets and provide a self-consistent product (a new ABSCO table) for use in the retrieval algorithm. CRDS data allow long-pathlength measurements with absolute intensities, providing both lineshape information as well as LM and CIA, however information on narrowing of the lineshape may be diminished in the saturated line-centers and no temperature dependent CRDS data are yet available. The FTS data provide intermediate paths, full band coverage and consistency across a broad pressure and temperature range. These spectra are all modeled with multispectrum fitting software using first the spectral line database HITRAN2012 [28], and then model values are adjusted and fitted for better agreement with the data. Limitations in the analysis of laboratory data are then identified and systematically treated using well characterized atmospheric datasets such as TCCON data in the A-band region recorded simultaneously with other atmospheric variables such as aerosol loading and precipitable water vapor. Section 3 of this paper presents the experimental and atmospheric datasets used in this process, followed in section 4 by the rationale and methodology; the results are tabulated, displayed and impacts on atmospheric retrievals are discussed in section 5 and conclusions are given in the final section 6.

3. Data

3.1. CRDS data

Measurements performed using the frequency-stabilized cavity ring-down spectrometer located at the National Institute of Standards and Technology (NIST) in Gaithersburg, MD, have been previously described [15, 17] and only the relevant conditions and pertinent calibrations are reviewed here.

The high reflectivity mirrors provide wavelength dependent absorption pathlengths of ~ 3.5 km that are precisely determined by measurements of the cavity finesse. The spectrum frequency axis is linked to the free-spectral-range (FSR) of the ring-down cavity which provides an extremely linear and precise frequency that can be accurately calibrated in terms of an external frequency reference, in this case a co-aligned potassium gas cell. The laser frequency mode selection is performed with a high precision wavemeter that provides ±30 MHz uncertainty, and uncertainties of the cavity mode position (< 0.5 MHz) and reference laser (< 0.1 MHz) are smaller than the probe laser linewidth (2 MHz).

For CRDS measurements, the measured ring-down decay rate (i.e. inverse decay time) divided by the speed of light yields the total optical-loss-per-unit length. Here, this quantity is modeled as the sum of three wavelength-dependent components: cavity mirror losses

(measured under empty-cavity conditions), Rayleigh scattering losses (calculated), and the absorption co-efficient of the medium. In the present experiments, depicted in Figure 1 and Table 1, the accuracy of the resulting absorption coefficient was limited not by the accuracy of the gas mixture (20.720(43)% O_2), but rather by uncertainties in the mirror losses (caused by drift in baseline etalons) and uncertainties in the mean decay time (caused by the finite signal-to-noise ratio of the ring-down decay signals). At relatively high optical depths, transmission through the ring-down cavity was substantially reduced below the measurement threshold, thus preventing measurements of decay times which were less than approximately 4 μs. This limited the dynamic range of the CRDS measurements and resulted in truncated profiles in spectral regions exhibiting strong absorption. The details of the CRDS recordings are given in Table 1.

Reduced spectra were provided for multispectrum fitting for which Rayleigh scattering effects were removed and the cavity loss was normalized to unit path. For introduction into the multispectrum fitting software these spectra were exponentiated and the units correspond to a pathlength of 10 km. Temperatures ranged from 295–298 K and no effort was used to stabilize or control the temperature of the cell. Typically, during the course of a single scan the temperature varied by about 0.1 K. Gas pressure was measured with two NIST-calibrated capacitance diaphragm gauges having full scale responses of 13.3 kPa (100 Torr) and 133 kPa (1000 Torr), respectively, and read-out uncertainties of < 0.01% and pressures varied about 0.03% over the course of a scan.

3.2. Laboratory FTS data

Several modifications to an absorption gas cell system configured to a Fourier transform spectrometer (FTS), Bruker IFS-125HR, at the Jet Propulsion Laboratory, were made to enable the collection of high quality oxygen A-band spectra. These modifications include an alternative light source, an external calibration gas cell and use of two different multipass, White-type cells (one operating at ambient room temperature and the other at selected colder temperatures).

To calibrate the wavenumber scales of all the scans, an extra vacuum chamber was configured to the Bruker in order to pass the NIR signal through a sealed 50.8 cm cell containing about 1 mPa (7 μTorr) potassium vapor at room temperature. A source module from an IFS-120HR FTS was configured in this extension chamber for input of NIR radiation through the external source window. An off-axis paraboloid mirror was used to collimate the radiation from a 100 Watt Tungsten filament bulb. A schematic depicting this chamber is given in Figure 2. At the exit of this cell a spherical mirror with focal length 304.8 mm was used to direct the beam into the FTS. At the resolutions available to this FTS (> 0.002 cm^{-1}) the hyperfine and isotopic features of the potassium (D_1, D_2) spectrum are important for accurate determination of the wavenumber calibration factor.

Transfer optics placed in the (left) sample compartment of the FTS are used to couple the NIR beam into either of two multipass cells, one a ‘Saturn class’ White cell purchased from Gemini Scientific Instruments, and the other a custom built coolable White cell originally constructed for far-IR studies at the University of British Columbia (UBC cell [32]) and used recently at JPL to study intensities of the ethane torsional band (ν_4) near 289 cm^{-1}

[31]. The Gemini cell consists of dielectric silver coated mirrors, optimized for 13000 cm^{-1} wavenumber region attached to endplates separated by a glass cylinder with vacuum seals. Micrometer adjustments enabled the total path to be adjusted between 82–115 m. The UBC coolable cell was designed for collision-induced absorption studies in the FIR and is capable of holding high density gases (< 253 kPa or 2.5 atm) at temperatures from 50–300 K. Using 0.05 mm thick polypropylene windows and gold mirrors the UBC coolable cell provides a maximum 60 m path.

Details of the UBC cell installed at JPL, and its operation can be found in Ref. [31], however, the temperature control was improved to enable better SNRs for the cold data. Initially, N_2 gas was flowed through copper tubing immersed in a dewar of $N_{2(l)}$ or $Ar_{(l)}$ to stabilize the flow rate and minimize sample liquefaction. However, better control was achieved for the last set of scans by cooling of the flow gas using a Brooks Polycold gas chiller. A slightly narrower temperature range (176–296 K) compared with [31] was also implemented due to the desire to model the Earth atmosphere. The SNR had been limited by use of liquid argon coolant that limited the stability of the cell temperature, which depended critically on 1) the gas flow rate, 2) the number of coils embedded in the liquid argon, and 3) the liquid level itself. Use of the Polycold gas chiller enabled stable temperatures over sufficient recording times to achieve SNRs of > 150. Two different silicon photo-diodes were utilized for recording of the FTS spectra. Initial data (all of the ‘Saturn class’ White cell data and several of the UBC cell scans) were recorded with the photo-diode delivered with the spectrometer, however the ability of this detector to pass the fast modulated signals in the NIR was observed to decay over some time, and the apparent zero signal level became unacceptably large. A replacement detector (which came with new preamplifier electronics as well) was found to have improved response time. A listing of the spectra used in the multi-spectrum fit are given in Table 1 and a typical air spectrum is shown in Fig. 3.

3.3. Atmospheric FTS data

TCCON is a network of ground-based FTS instruments that record direct solar spectra in most of the near-infrared, including the OCO-2 spectral bands. The TCCON site in Lamont, Oklahoma, is co-located with the Southern Great Plains (SGP) site of the DoE Atmospheric Radiation Measurement (ARM) program. The SGP facility operates a range of instrumentation, including the Normal Incidence Multifilter Radiometer (NIMFR), used to derive aerosol optical depths from solar radiation at multiple wavelengths.

To provide CIA information across the span of the oxygen A-band directly from well-characterized atmospheric data, a method was developed to analyze the variation of solar direct beam measurements with solar zenith angle for deduction of CIA using atmospheric data. Data selection for this method is critical such that data from periods of time with reasonably stable aerosol and precipitable water vapor (PWV) are utilized while also spanning a range of atmospheric path lengths. To ensure satisfactory conditions, the method combines remote-sensing datasets from the TCCON [11] and NIMFR instruments co-located in Lamont, Oklahoma, as well as ARM data products that specify the temperature and moisture profiles at SGP.

Several criteria were used to select satisfactory time periods on days between January and July 2012 for analysis: (1) the time series of solar irradiance from NIMFR is consistent with clear skies (cloud free); (2) radiance measurements in the OCO-2 bands are reasonably stable; (3) the precipitable water vapor (PWV), as computed by a retrieval from an ARM microwave instrument [33], varies by less than 10% over a given time period; (4) the aerosol optical depth (AOD) derived from the NIMFR in its 11532 cm^{-1} channel varies by less than 10%; and finally (5) the water vapor airmass factor m_w has a range (max − min) exceeding 1.5. The m_w is taken as defined by Kasten (1966) as:

$$m_w = [\cos\theta + 0.0548(92.65 - \theta)^{-1.452}]^{-1} \quad (1)$$

where θ is the solar zenith angle in degrees. From the six month interval, 13 cases were selected for analysis and further filtered to eliminate spectra from consideration if its measurement time coincided with an outlier (more than 20% different than the median for the case) in either the PWV or the AOD measured by the NIMFR.

Both the FTS and NIMFR measure a portion of the solar energy and track the sun, but at differing amounts of collected radiation and with different tracking mechanisms. Comparisons between FTS and NIMFR measurements in a transparent spectral region common to each instrument (11532 cm^{-1}) indicated that while the NIMFR data showed smooth temporal behavior, the TCCON FTS data did not. We ascribe this to a solar tracking issue in the FTS. To remedy this issue, a correction procedure that scales an entire TCCON FTS observation, $R(\sigma)$, to match the effective irradiance of temporally matched NIMFR irradiances, was developed. First, a scale factor is obtained for each FTS spectrum by dividing the NIMFR irradiance at 11532 cm^{-1} by the FTS observation after the NIMFR instrument function for this channel had been applied. This irradiance ratio is then used as a scale factor and applied to corresponding FTS spectra, thereby tying the TC-CON data-set to the more stable NIMFR. This scaled irradiance is crucial for binning and sub-sampling the data based on the water vapor airmass factor. For each candidate day of recorded atmospheric spectra, a linear fit to the values of ln [R(11532 cm^{-1})/R_{ref}(11532 cm^{-1})] vs. m_w is performed. Here R is the FTS measurement and R_{ref} is a fixed value (such as the greatest value of R(11532 cm^{-1}) for that date). This line is then binned into m_w groupings of size 0.5. We then find the value of R/R_{ref} in each bin closest to the fitted least squares line, and eliminate all other spectra from this case. This vetting process eliminates points that are far from the ideal air mass×vertical optical depth due to instrumental noise and/or aerosol extinction and gives the data the best possible value of vertical optical depth for subsequent determination of unexplained optical depths. Figure 3.3 provides an example of this procedure for one of the chosen days.

4. Analysis

4.1. Calibrations

High accuracy spectroscopic methods generally require primary or secondary calibration methods to account for known biases in the measurements. Calibrated pressure gauges

(MKS) and platinum resistance thermometers were employed in each experiment, and individual measurements were not limited by the accuracy of these gauges. Shortly after the experiments using the UBC 'cold' cell, a secondary set of gauges was measured with respect to the gauges in this study, then the second set was sent for calibration. The resulting secondary calibration indicates that the primary gauges have maintained the stated accuracy of 0.25%.

Frequency and intensity calibration of the CRDS data were described in the prior section since calibrated data were provided for this study. For the FTS data, the multispectrum analysis software [34] was used to empirically adjust the measured wavenumbers, σ_{meas}, and determine the calibrated wavenumbers, σ_{cal}, based on the positions of the potassium D_1 (12985.1 cm^{-1}) and D_2 (13042.9 cm^{-1}) lines. Although the hyperfine and isotopic line positions of the D_1 and D_2 potassium features were well characterized by saturation spectroscopy [35], a complete listing of position *and* relative intensities was not found in the literature. For the software (described in the following section) it was necessary to create a listing of the calibration gas features in HITRAN format (see Supplemental material). With focus on the D_1 and D_2 residuals, the potassium gas pressure and the wavenumber scaling factor d_1 (see Eq. 2) were manually adjusted to minimize these (only these) residuals.

$$\sigma_{cal}=(1+d_1)\times\sigma_{meas}+d_2 \quad (2)$$

Values of d_1 varied from -4×10^{-8} to $+3\times10^{-8}$ for the room temperature scans in the Gemini White cell and were all -26×10^{-8} or -30×10^{-8} for the UBC cell, d_2 was not useful and kept at zero. Variation in the intensity of the potassium absorption was observed since the vapor pressure is strongly temperature dependent, however the low pressure ensures that this variability did not produce any significant pressure shifts. Absolute uncertainties on the calibrated FTS wavenumber scale are about 4×10^{-8} relative, or roughly 6×10^{-4} cm^{-1} absolute (20 MHz).

Some FTS intensity data are not treated explicitly with Beer's law, such that not all contribute to absolute intensity determination. In particular the spectra recorded with the impaired photo-diode required significant (fitted) zero-offsets, Z, where transmissions across a given spectrum T_i are modified $T_i^{'}=T_i+Z$. Spectra recorded first with the 'Saturn class' White cell required −0.5%–−0.9% offsets, and the three spectra retained from the first set of data with the UBC White cell required −2.0% to −2.3% offsets. After replacing the detector, fitted values of the zero offset were within the noise level (0.5%) and are essentially zero. Six of these spectra did have the zero-offset fixed at zero, indicating that their transmission depths (like the CRDS data) are considered absolute by the fitting program.

4.2. Line mixing model

The comprehensive study of high-pressure oxygen A-band spectra reported by Tran, Boulet and Hartmann [22, 36] included a theoretical derivation of the collisional relaxation matrix based on the infinite-order sudden (IOS) approximation followed by the energy correction sudden (ECS) to the off-diagonal elements [37] as used for CO_2 by Niro *et al.* [38].

Application of the standard angular momentum formulation required the molecule to be approximated as a pure Hund's case *b*, such that a spin-free ECS model, in which the collision rates and scaling lengths were fitted to the line-broadening values, was given. The IOS/ECS formalism allowed for adjustment of the scaling length's for both O_2-O_2 and O_2-N_2 collisions. The results of the fitting at several temperatures enabled modeling of the off-diagonal elements with a power-law expression. The full matrix of values computed for the air mixing ratio (X_{N2} = 0.79, X_{O2} = 0.21) is available as supplemental material in Ref. [22], and the O_2-O_2 relaxation matrix was provided on request. These two matrices were then utilized to (back) calculate the N_2-O_2 relaxation matrix using the binary mixture formula.

4.3. Data model

The spectroscopic datasets of this study vary widely in pressure and temperature, but the data are focused narrowly on gaseous oxygen absorption (both resonant and non-resonant) in the presence of itself as well as nitrogen gas. In order to provide a self-consistent spectroscopic model capable of high-fidelity reproduction of atmospheric data, we have fitted the data with both a line-by-line (LBL) spectral lineshape model as well as augmented this model with approximate effects of line mixing and collision induced absorption. The multispectrum fitting program contains a number of different spectral lineshape models, as well as options for effective (Rosenkranz [39]) line mixing or full (W-matrix) line mixing.

4.3.1. LBL parameters—Positions and intensities of the oxygen A-band transitions are partially fitted within the analysis. Unlike the broadening, shift and narrowing parameters, the line positions and intensities are well defined quantum-mechanically and expressions that allow interpolation/extrapolation as well as information from other analyses can be confidently employed to improve the physical representation of the data within the model. For zero-pressure line position determinations, a simple Taylor series defining the upper state [$^1\Sigma$ (v = 0)] energies (Eq. 3) based on the term value, rotation, and centrifugal distortion parameters was provided to the fitting routine via definitions of auxiliary parameters and mathematical operations.

$$E'(b^1\textstyle\sum_g^+, J') = G_0 + B_0 J'(J'+1) - D_0 J'^2 (J'+1)^2 + H_0 J'^3 (J'+1)^3 \quad (3)$$

The definitions of B_0, D_0 and H_0 as auxiliary parameters enable the fitting program to determine their values from the spectral data during the fit. Lower state energies for all transitions of O_2 in the $^3\sum_g^-$ state are taken from [40] based on the extended analyses presented by [41] and vetted by [42, 43]. Line positions are then determined by differences between upper and lower state energies: $\sigma_0(J', E'') = E'(J') - E''$. Small, but significant deviations in E'' at $J > 20$ in comparison to HITRAN2012 result in changes to B_0, D_0, and H_0 outside the reported error bars, even though the determined positions agree within a few thousandths of a wavenumber. The change in lower state energies with respect to HITRAN2012 is depicted in Fig. 5. The divergent groups of flat triplets above $N'' = 20$ observed in this plot indicate the difference in the models lies in the rotational expansion and

that the spin-splittings of the two parameterizations are in closer agreement, very small deviations at all N'' are observed due to the truncation of E'' to four significant figures in the database.

Intensities of transitions between $^3\Sigma$ and $^1\Sigma$ states were described by Watson [44] and the necessary lower state B_0, λ_0 and γ_0 parameters were adopted from [41] for the calculation of the Hönl-London factors (S_{HL}). The general expression for intensity includes the empirical Herman-Wallis terms [14, 45] c_1 and c_2:

$$I(J,m,T)=G_{ev}\sigma_0 S_{HL}(J)(1+c_1 m+c_2 m^2)e^{-E''/kT} \quad (4)$$

Where m is equal to $-J''$ in the P-branch and $J''+1$ in the R-branch. The parameter, $G_{ev}=\frac{8\pi^3\mu_{SO}^2}{3hcQ_{evrs}}$, is independent of the quanta and is a determinable 'band parameter' along with c_1 and c_2. The line intensity depends further on the effective spin-orbit coupled magnetic dipole (μ_{SO}), the total electronic, vibrational, rotational and spin partition sum (Q_{evrs}) as well as fundamental constants h (Planck's constant), k (Boltzmann's constant) and c (speed of light). The upper state dependence of the Boltzmann factor has been neglected. Together these values give the band intensity, $S_b(T)$, *via* summation over all of the transitions.

A speed-dependent Rautian lineshape model is chosen for the resonant oxygen lines of the main isotopologue. This formalism incorporates speed-dependence as a correction to the Voigt lineshape. The real part (Eq. 5) is used to determine collisional effects inherent to a given transition:

$$F(x,y,S,H)=\frac{2}{\pi^{3/2}}\int_{-\infty}^{+\infty} v e^{-v^2}\arctan\left[\frac{x+v}{y(1+S(v^2-\frac{3}{2}))+H}\right]dv \quad (5)$$

in which the frequency detuning relative to the shifted line center (x), as well as the Lorentz width (y) are parameterized for evaluation as an integral through velocity (v) space with the speed-dependence parameter S implicitly included [46, 47] and Dicke narrowing (H) optionally included. The variables x, y and v are all dimensionless in this formalism, where x (relative distance to line center) and y (line width) are divided by the Doppler width (γ_D) and multiplied by $\sqrt{(ln(2))}$ for the spectral line and v is divided by the average speed (most probable velocity). This expression omits the far-wing effects of the finite collision time described by Ciuryło [47], as well as the speed-dependence of the shift (which would show up in the asymmetric portion described in the following section), but there has been no evidence to suggest these effects are significant for the O_2 A-band. Ciuryło refers to this expression as the speed-dependent asymmetric Voigt profile (SDAVP), and our omission of negligible terms is similar to other formulations of the speed-dependent Voigt profile [48, 49] and the formulations are expected to be mathematically equivalent. The integral is evaluated numerically over a grid of velocities from $v=-4$ to $+4$ in sixteen steps, this sampling is sufficient for reproduction of spectra at SNRs of up to 200:1 such as those used

in this study. Numerical testing has shown that the approximation fails in different limits for the real and imaginary parts (next section). For the real part the failure occurs far from line center at very long pressure-pathlengths not typically encountered in experimental data. In the fitting algorithm, speed-dependence is applied to the *total* shifted frequency and Lorentz width as calculated from the self and foreign broadened/shifted components. Transitions due to minor isotopologues and potassium transitions that do not require speed dependence are given the simplified Voigt lineshape, equivalent to Eq. 5 with $S = 0$. However, a different algorithm is applied for the simple Voigt calculation [50].

Separation of the components of the line shift into pressure and temperature dependent components is given by:

$$x=(\sigma-\sigma_0-p\,[X_f\,(\delta_f+(T-T_{ref})\delta_f^{'})+X_s\,(\delta_s+(T-T_{ref})\delta_s^{'})])/\gamma_D \quad (6)$$

where σ is the frequency at which the lineshape is to be determined, σ_0 is the center (rest) frequency of the transition; p is the pressure; X_f and X_s are the mole fractions of the foreign and self broadening gases respectively; δ_f and $\delta_f^{'}$ are the foreign pressure shift at the reference temperature T_{ref} = 296 K and foreign pressure shift temperature dependence, respectively; δ_s and $\delta_s^{'}$ are the self pressure shift at T_{ref} and self pressure shift temperature dependence, respectively; and γ_D is the Doppler width of the transition. Similarly the pressure and temperature dependence of the Lorentz broadening component of the lineshape is given by:

$$y=(p\,[X_f\gamma_f(T_{ref}/T)^{n_f}+X_s\gamma_s(T_{ref}/T)^{n_s}])/\gamma_D \quad (7)$$

where γ_D, p, X_f and X_s are as defined in Eq. 6; γ_f and n_f are the foreign pressure broadening at T_{ref} and its exponential temperature dependence, respectively; and γ_s and n_s are the self pressure broadening at T_{ref} and its exponential (power law) temperature dependence, respectively.

The reference temperature of 296 K is chosen to make parameters compatible with the HITRAN database, however, the parameters S, n_s, δ_s, $\delta_s^{'}$ and $\delta_f^{'}$ are not part of the traditional HITRAN parameter set. Fortunately, such parameters can now be incorporated into the recently released *HITRANonline* database [51], in which extensible formats (such as the Rautian) that are consistent with the Hartmann-Tran profile [52] can be accommodated.

These LBL parameters are defined explicitly for every database entry given in the fitting program. The program computes the contribution of each line to the optical depth of each spectrum and sums the values prior to the transmission calculation as shown in Eq. 8.

$$\kappa_i = \varrho_{O_2} \sum_{j=1}^{N} F_j(x_i, y, S) I_j(J, m, T) \quad (8)$$

Where the absorption coefficient κ_i is determined at the ith frequency (σ) for all j of the N lines given in the LBL and within a cutoff criterion. The absorption is then converted to transmission using Beer's law; $T_i = e^{-L\kappa_i}$, using the pathlength, L, and oxygen number density, ϱ_{O_2}, for direct comparison to experimental data. Many of the LBL parameters are not determinable, or correlated with each other and thus inter-dependent, these values may be either fixed to zero or to some reasonable value such as values from the HI-TRAN2012 database. The lineshape parameters are, in particular, subject to augmentation by the effects of LM, which are accounted for outside the LBL database.

4.3.2. Line mixing—In general transitions involving only the same isotopologue can become 'mixed' during the absorption process due to collisional transitions that change the angular momenta of the initial and/or final states. When collisional transition probabilities are low, such that the average energy transfer does not span the distance between transitions, the process is well approximated by line broadening as described by the Lorentzian width given in Eq. 7. However, at high enough pressures where the Lorentzian width becomes comparable to the distance between adjacent transitions the collisional transitions cause line dispersion, with intensity shifting toward the stronger line. Generalized across a band the effect can significantly alter the band-shape at high pressures.

The amount of line mixing between transition j and transition k can be described using a complex matrix formalism in which the entire relaxation matrix **W** represents the fully coupled collisional broadening and shifting across a set of transitions; defined with the complex diagonal elements $W_{kk} = y_k + ix_k$, and imaginary line-coupling off-diagonal elements, $iW_{jk} = ie^{-E_j''/kT} e^{E_k''/kT} W_{kj}$, which produce the dispersion at a given pressure and temperature. An implicit transformation of coordinates in Liouville (line) space removes the **W** matrix dependence on line positions with the vector σ_0 removed as $\mathbf{G}(\sigma) = \sigma - \sigma_0 - i\mathbf{W}$ [53]. The amount of dispersion, Y_k of a given line k within the mixed set is dependent only on **G**, as well as the intensities $I_j(T)$, which further depend on state populations at a given temperature, such that the temperature dependence of **W** must account for detailed balance. The ρ vector contains the populations, $\rho_j(T) = e^{-E_j''/kT}$. Intensity information is placed in the vector **X** such that $X_j = \sqrt{I_j/\rho_j}$. The full effect of the relaxation matrix on the Lorentz component of the cross section can be written succinctly in matrix form as $Y = \frac{1}{\pi}\mathrm{imag}\left[\mathbf{X}^{\mathbf{T}}\mathbf{G}^{-1}\rho\mathbf{X}\right]$, however the real portion is already diagonal making full complex matrix manipulation unnecessary. Instead, following [54], the eigenvectors **A** obtained from diagonalization of the imaginary part of **G** are used to obtain Y_k at a given temperature.

$$Y_k(T)=imag\left[\sum_{j=1}^{N'}\mathbf{X^T A}+\rho\mathbf{X A^{-1}}\right] \quad (9)$$

provided that the lines within a mixed set of N' transitions have their cross-sections evaluated together, the entire band intensity is preserved. The dispersive effects of each $Y_k(T)$ multiply the imaginary portion of the lineshape:

$$F'(x,y,S,H)=\frac{1}{\pi^{3/2}}\int_{-\infty}^{+\infty}ve^{-v^2}\ln\left[1+\frac{x+v}{y(1+S(v^2-3/2))+H}\right]dv \quad (10)$$

which is calculated along with $F(x, y, S)$ using the LBL parameters. The absorption coefficients are then determined within a mixed set as:

$$\kappa_i=\varrho_{O_2}\sum_{k=1}^{N'}[F_k(x_i,y,S,H)+Y_k(p,T)F_k'(x_i,y,S,H)]\,I_k(J,m,T) \quad (11)$$

Remaining transitions outside the mixed set are calculated as before and the total cross section is computed for each spectral element of each spectrum.

An extensive theoretical basis for oxygen LM was published in [22, 36] which incorporates an infinite-order sudden approximation of the relaxation matrix. With 66 resonant transitions included in this analysis of the A-band spectrum, the incorporation of theory to determine the 66×66 elements of **W** is essential, especially since the theory indicates that the nearest neighbor approximation (in which a sparse tri-diagonal matrix can be utilized) does not hold for oxygen LM. Rather, the largest off-diagonal elements alternate within the P and R branches, corresponding to strong J-coupling within the ${}^{P}P,{}^{P}Q,{}^{R}Q$ and ${}^{R}R$ sub-branches. Furthermore, spin-couplings between spin-states (*i.e.* within a ${}^{P}P-{}^{P}Q$ or ${}^{R}Q-{}^{R}R$ doublet) are also not negligible, and carry the opposite sign compared to the J-couplings.

For use of the LM from [22, 36] an I/O routine was written that incorporates the lower-triangle of **W** into the input file. A schematic representation of the matrix is given in Fig. 6. Since about 5% uncertainty exists for the accuracy of **W**, a scaling factor, adjustable by the user at run-time, was incorporated on the off-diagonal elements through definition of auxiliary parameters and constraints in the input file, this also allows for scaling factors due to differing LM formulations. A test output from within the LM subroutine confirmed that the detailed balance calculation reproduces the upper-triangle of **W** and that a sign change for the **W** matrix is necessary to account for a differing definition of the imaginary portion of the relaxation matrix and the derived Rosenkranz parameters. The sign change is consistent with the sign change in the 're-normalization' process [38] applied in Tran's code that is provided along with the **W** matrix, the factor of $\frac{1}{2}$ is a difference in empirical scaling that will be described in more detail later. Further reconciliation of the theoretical LM with

the experimental and atmospheric data necessitated the parsing of the theoretical LM into sub-branches in which spin-couplings are optionally removed. The sub-band matrices allow connections of all even ΔJ values.

For this oxygen band, at the sensitivity for which LM becomes relevant, CIA also becomes important [30], so an integrated approach is important to retrieval of self-consistent LBL, LM and CIA.

4.3.3. Collision Induced Absorption—The nature of CIA in the oxygen molecule has been debated for almost a century ([55]), and the most detailed work on oxygen has focused on optical regions where resonant transitions are not found. However, it is generally accepted that CIA exists as a < 10% component (at 1 atm or 101.325 kPa) in regions of resonant absorption as well, especially when the absorption bands are weak, such as the triply forbidden $^3\sum_g^- \rightarrow {}^1\Delta_g$ band near 7900 cm^{-1} [56]. In the A-band region, the CIA was estimated by Tran, Boulet and Hartmann [22] to be 1% of the resonant absorption at 1 atm (101.325 kPa). In that study, very high pressures (> 10 atm) were utilized to determine the CIA as a leftover contribution from the resonant line absorption where LM has been explicitly included. The accuracy was limited to 5% due to uncertainties in the theory as well as the inherent difficulties of modeling overlapping transitions. Later, Long *et al.* [23] performed laboratory measurements (building on those used here) and showed that the CIA of Tran, Boulet and Hartmann [22] was underestimated in the strongest part of the P-Branch. The present work focuses on the atmospheric pressure range, in which the effects of resonant lines still dominate and LM and CIA manifest at or near the noise level of both the laboratory and atmospheric data.

Due to extensive pathlengths, the CRDS and TCCON data are most sensitive to the CIA. In the 131 kPa air CRDS data, up to 4% 'unexplained' absorption is observed when incorporating a model without CIA. The 53 kPa air CRDS data also contains up to 1% 'unexplained' absorption. The presently used CRDS datasets span only the P-branch, but the high airmass TCCON data are also sensitive to CIA, and thus we have evaluated improved CIA models using both datasets.

For proper analysis of the LBL and LM parameters using the 53 kPa and 131 kPa CRDS data, it was essential to include an adequate CIA model within the multispectrum fitting program. Since the CIA derived by [22] disagreed with the NIST data across the band, we developed a flexible model based on the resonant line positions to approximate the shape of the 'unexplained' absorption in both the CRDS and TCCON data. Recognizing the pseudo-Boltzmann band contours in the feature prompted the use of the entire list of A-band positions and intensities convoluted with a broad Lorentzian to produce a 'CIA' that is similar to the resonant band contour (and completely *ad hoc*). Although useful in the limited range and sensitivity of the current CRDS data, this CIA model was inadequate for describing the non-resonant absorption in the vicinity of the R-branch bandhead and the gap between P and R branches as observed in the atmospheric data set. Nevertheless, the multispectral fitting software was provided with the capability for generic input of CIA in binary pairs (gases X, Y) as either Gaussian or Lorentzian features (with a list of positions,

widths and intensities) that sum up to give a binary nonresonant absorption, $\alpha(\sigma)_{XY}$ at a given wavenumber, σ. This allowed fitting of CIA sensitive data with a reasonable approximation in place during optimization. For this work approximate CIA for pure O_2 and N_2-O_2 are treated with the partial number densities (ϱ_X) factored in:

$$\alpha(\sigma)=\varrho_{O_2}\varrho_{N_2}\alpha(\sigma)_{O_2N_2}+\varrho_{O_2}\varrho_{O_2}\alpha(\sigma)_{O_4} \quad (12)$$

Where the N_4 contribution is neglected. With this empirical model the CIA at each and every experimental data point is calculated prior to the least-squares fitting routines, and the effects of the CIA are folded into the transmittance:

$$T(\sigma)=Z+B(\sigma)e^{-[\varrho_{N_2}\alpha(\sigma)_{O_2N_2}+\varrho_{O_2}\alpha(\sigma)_{O_4}+\kappa(\sigma)]\varrho_{O_2}L} \quad (13)$$

where the background across a spectrum is represented generally by a Chebyshev polynomial, B, and the total transmittance T contains this polynomial as well as the CIA and resonant line information, Z is the zero offset used on some of the FTS spectra and as a piece-wise balancing factor in CRDS spectra that required corrections to approximate CIA models used in the line-by-line parameter fitting. Since the CRDS data are corrected for scattering losses, the transmission profile is background free, and the polynomial, $B(s)$, is unity. Although the effects are minor in the shorter path FTS data, the CIA correction can remove the need for higher order baseline polynomials that would otherwise fit any trace of CIA in these spectra.

With the CRDS data limited to the P-branch, the effects of CIA in the R-branch are better understood by examination of the 'unexplained' absorption in the TCCON data described in Section 3. For determination of this CIA, the LBL+LM model from this work was used to generate a 'resonant-only' version of the ABSCO table. Using the set of TCCON spectra described in section 3 we then determined the total vertical optical depth as a function of wavenumber from the variation in the measurements with atmospheric path as the solar angle changes. Using the sub-sampled time series of $R(\sigma)$ (the TCCON FTS measurements at wavenumber σ) and their corresponding airmass factors m_w, the total vertical optical depth is given by the slope of the linear fit of log $[R(\sigma)/R_{ref}(\sigma)]$ vs. m_w, where $R_{ref}(\sigma)$ is a fixed value. These vertical optical depths are a starting point for the remaining work, namely the determination of the (as yet) unmodeled absorption due to oxygen collision pairs. The procedure then is to subtract optical depths (ODs) of the known extinction sources from the derived vertical optical depths, thereby obtaining optical depth values from the unmodeled absorption sources.

The calculated ODs, which are the sum of the O_2 line ODs from the LBL and LM data analysis described thus far (excluding the empirical CIA) and the ODs from other molecular sources (including Rayleigh scattering) computed by the Line-By-Line Radiative Transfer Model (LBLRTM) [57], are subtracted from the ODs. To remove the contribution of aerosols in the A-band, for each case a spectral Angstrom relation is fitted to this difference at wavenumbers just outside of the O_2 A-band (12800 cm^{-1}) – 12950 cm^{-1}), 13250 cm^{-1}) –

13400 cm^{-1}). (See cyan line in Fig. 7). These spectral aerosol optical depths (AODs) are subtracted from the previously computed differences, resulting in a spectrum of unexplained optical depths (UODs), which are associated with the A-band CIA.

We then bin the UODs in the 13000–13200 cm^{-1} region in 1 cm^{-1} intervals, with roughly 130 spectral points each, and filter the values statistically. Sharp features due to issues with the resonant line (LBL+LM) model are ignored after this filter. Within bins in which 70 or more of the UOD values fall in a narrow range, these comparable values are averaged. Some bins with wider distributions of points are required to have more samples within a wider range. Due to the lower sampling in the latter case, these points (such as the values near $5x10^{-7}$ cm^{-1}/am^{-2} in Figure 8) are weighted less in the determination of a smooth final product. If there are fewer than the looser standard number of points in a bin, there is no representative UOD value for that wavenumber. Fig. 7 shows the elements of the procedure used in the A-band for one case; the magenta points are the representative points resulting from this filtering approach. Figure 8 shows the representative points determined from all 13 representative TCCON data sets that clear the specified cloud, AOD, and PWV conditions. Note the evidence of a possible modeling issue near strong lines, e.g. 13075, 13190, and 13162 cm^{-1}.

We then compute the median value of the UODs for bins with at least three (out of the 13 possible) UOD values. We obtain associated O_2-air binary absorption coefficient (a, $cm^{-1}/amagat^2$) by dividing the representative UODs by the sum of the product of the O_2 and air column amounts (in density units). Since the 1 cm^{-1} binning used to obtain the UOD values is somewhat arbitrary, we manually review each value, resulting in occasional adjustments to both the absorption coefficient and the wavenumber value with which it is associated. Finally, absorption coefficients near strong lines that are likely to have been impacted by the modeling issue mentioned above are removed from the analysis. The final set of absorption coefficients are shown as filled green circles in the Fig. 8. A smooth curve (green curve in Fig. 8) is fitted through these points, providing the final O_2 CIA coefficients implemented in the MT CKD and ABSCO continuum model.

5. Results and Discussion

An iterative process, both within and external to the multispectrum fitting, was required for full incorporation of the LBL+LM+CIA model described in the last section. First iterative results from incorporation of LM and CIA resulted in a new self-consistent LBL+LM+CIA model, and then the LBL+LM portion of this model was tested to derive modified CIA from the TCCON data set. Testing of variables revealed that five band parameters, G_0, B_0, D_0, H_0 (where the subscript indicates the ground vibrational level of the $^1\Sigma$ excited state) and G_{ev} were determinable along with LBL parameters for width, shift: γ_f, γ_s, δ_f and δ_s for J values ≤30 and LBL parameters for temperature and speed dependence: n_f, n_s, δ'_f, δ'_s and S for $J \leq 23$. Some pressure shift parameters for the $^{18}O^{16}O$ isotopologue were also floated to minimize residuals further, however it was clear that some issues with the lower state energies and or line positions of these features could not be quickly rectified and these parameters are not reported here.

Initial iterations fitted the CIA effects in the CRDS and FTS data with effective background parameters. The effective backgrounds for the CRDS data could then be used to determine the shape of the CIA as described earlier. The CIA shown in Fig. 8 are the absorption coefficients from (red) [30], (blue) [58], and the (black) values from Tran [22] that are included in HITRAN2012. Our derived values (green) in the A-band P-branch at 13100 cm^{-1} are in 20% lower compared to Long *et al.* [23] and the CIA of Spiering *et al.* [58] is 50% of our value at the same wavenumber, however the three data sets converge somewhat at lower wavenumbers and only agree with Tran *et al.* near 13075 cm^{-1}. Unlike Tran *et al.* the new CIA in the R-branch rapidly drops near the band-head, but does not go to zero. Coupling between these effective backgrounds and the LM was observed and several iterations through the CIA model were performed. The dominant effect of LM was seen in the LBL parameters near the *R*-branch band-head, which showed erratic *m* dependences. A scale factor of 1/2 was found to dampen the erratic *m* dependence and significantly reduce curvature between transitions in residuals at high pressures. Unfortunately, this LM also introduced some curvature in the CRDS residuals that could not be compensated with LBL or CIA. Furthermore, comparisons with TCCON data revealed that this augmented LM was inadequate for describing the precipitous drop in absorption at the band head (near 13165.3 cm^{-1}, see Fig. 9). The high pressure FTS data have insufficient SNR to describe the nearly three order of magnitude drop in intensity from the nearest peak ($R29Q30$), which does not saturate in the laboratory spectra, and is absent from low temperature data. Previous success in this region with the models provided by Tran *et al.* [22] indicated that our empirical adjustment of LM required better metrics at the band-head. The TCCON data had been well modeled with the ABSCO 4.2 absorption coefficient table which is based on [14], [21], [22] and other information. Therefore, a segment of the ABSCO 4.2 table from 13165–13190 cm^{-1} at 107 kPa (803 Torr) and 293 K was placed into the data set as a diagnostic tool. Unfortunately, tests with various LM factors and fits of individual components produced frustrating incompatibilities between this model and in-band LM from FTS (depicted in Fig. 10). The LM matrix provided by Tran, Boulet and Hartmann contains every possible connection between each A-band transition, and it was determined by trial fitting that connections between the ^{R}R and ^{R}Q sub-bands were introducing residuals into the band-head and band-center regions that were absent when these values were omitted. Omission of all sub-band connections allows one to define the LM with four separate and considerably smaller matrices. Because the intra-subband elements were already the largest values, the remaining portions of the matrix (shown schematically in green in Fig. 6) contain over 90% of the matrix elements by magnitude, but contain none of the spin-changing terms. The four matrices, one each for ^{P}P, ^{P}Q, ^{R}R, and ^{R}Q are either 18×18 for RR and PP or 17×17 for ^{R}Q and ^{P}Q. By definition these submatrices cannot connect transitions of different spin, which is similar to saying all of the odd ΔJ elements in the **W**-matrix are negligible. This assumption that spin-changing collisions are negligible is not justified by theoretical arguments about the propensity for spin-changing collisions in relation to rotation-changing collisions [59]. In both the ground state study of [59], as well as Tran *et al.* [22] models of the odd ΔJ elements are about 10% of the magnitude of the even ΔJ elements. However, both studies ignored the spin-splitting of the $^{3}\Sigma$ ground state (about 2 cm^{-1}), which presumably would further decouple spin states and de-emphasize the importance of odd ΔJ elements. The sub-matrices utilized in the fitting program are provided in the supplemental material.

The even ΔJ elements of the LM, were fixed during optimization of the LBL parameters. Positions and intensities of each transition are defined by the parameters listed in Tables 2 and 3, as well as the lower state energies from Ref. [40]. A comparison of band parameters from this study and the recent work of Yu *et al.* [40] is presented in Table 2.

The comparison of line positions in Fig. 11a shows that most positions are systematically shifted from HITRAN2012 by 0.0002 cm^{-1}, a value just above the accuracy of the CRDS measurements and within the calibration accuracy of the FTS data. Since HITRAN2012 is based on average positions from mutliple low pressure CRDS measurements, there are several possible reasons for this small discrepancy (1) inaccurate FTS calibrations are biasing the result; (2) the selected CRDS spectra are on the high end of the mean used for HITRAN2012; (3) pressure shifts were not entirely accounted for in the HITRAN2012 positions. With the discrepancy so near the accuracy of the present data sets, we refrain from conjecture as to the source at this point and maintain that 15 parts per billion knowledge of absolute position is sufficient for remote sensing retrievals. Perhaps the most important aspect of the issue is that the positions and pressure shifts are attained in a self-consistent manner from sufficiently accurate data. Further inspection of the line-position differences reveals that *P*-branch values ($m > -30$) deviate from HITRAN2012 by less than 0.0003 cm^{-1}, still near the accuracy of the data. However, in the *R*-branch a somewhat larger divergence is observed with a $\succ$0.0006 cm^{-1} difference at $m = 30$. This asymmetric behavior was only observed when the lower state energies of Yu *et al.* [40] are utilized, whereas fitted positions using lower state energies from HITRAN2012 (not shown) produce a balanced residual pattern, a very large *H* value and a significantly different *B* value. Fig. 5 shows that lower state energies from HITRAN2012 deviate from Yu *et al.* [40] systematically by $>$ 0.001 cm^{-1} for $|m| > 25$, and many common lower state energies disagreed for matching *P*- and *R*- branch transitions in HITRAN2012. It seems that the HITRAN2012 positions were calculated based on fitted *P*-branch values and these mismatched lower state energy values produced a slightly inaccurate prediction of *R*-branch positions above $m = 25$. Although the transitions affected are beyond the Boltzmann peak, these are exactly the same transitions that participate strongly in LM near the bandhead and attempts to fit/scale LM prior to fixing the lower state energies to Yu *et al.* were largely unsuccessful. The Hamiltonian constraints combined with consistent lower state energies forces consistency among both upper and lower state energies and does not allow an asymmetric residual associated with (poorly modeled) LM to be adjusted via line position without a consequence elsewhere in the band. The fitted values for *B, D* and *H* (see Table 2) were in much better agreement with band parameters reported by Yu *et al.* [40] once the lower state energies were corrected to agree with Yu *et al.* The precision of *B* is higher than that given by Yu *et al.* [40], and the present value lies about 3σ from that value. The presently determined distortion parameter, *D* is of lower precision, and lies 25 σ from Yu *et al.* [40]. The lack of precision in *D* and significant deviation from the other study are likely caused by the extra degree of freedom from the present determination of *H. H* was fixed in Yu *et al.* [40] based on relations between the Dunham parameters, its value here has the same sign and is about 5$\times$ smaller. Uncertainties listed in Table 4 are precisions and do not reflect potential systematic errors; *e.g.* line positions uncertainties become as small as 1×10^{-5} cm^{-1} (0.3 MHz), whereas the frequency calibrations of the FTS data are 6×10^{-4} cm^{-1} (20 MHz) and frequency measurement in the

CRDS dataset has an accuracy closer to 6×10^{-5} cm^{-1} (2 MHz). The deviation from HITRAN2012, which is based on CRDS data utilized in this analysis, is close to 2×10^{-4} cm^{-1} (6 MHz) across much of the band.

Figure 11b depicts the intensities on a log scale. Relative intensities up to $|m| = 35$ from this study in comparison to HITRAN2012 deviate by less than 0.1%, however there is a systematic offset of 0.5% that results from the implicit inclusion of LM and CIA during the fitting process. It was found that the variation of distortion of the transition moment, c_1 and c_2 degraded the extrapolated values of the positions and intensities, so these values were held fixed at those determined by [14], who included both CRDS *R*-branch data, as well as high *J* intensity data from the *P* branch in their analysis. Fixing these values might indicate that relative intensities would have no standard deviation, however the lower state energies are systematically different and these affect the relative intensities at a fine level. With only one adjusted parameter, the relative intensities and the uncertainties of the intensities are all strictly related by Eq. 4 and a very high absolute precision ($< 1\times10^{-4}$) is attained. There have been many determinations of the intensity of the oxygen *A* band, and Table 3 outlines a few of the more recently reported values. The table includes determinable band values, as well as integrated band intensities and effective magnetic moments. These are all essentially interchangeable quantities, but have non-trivial interconversions that involve the partition sums, definitions of Hönl-London factors, isotopologue abundance (*a*), and odd units (1 Debye = 3.33564×10^{-30} C m = 0.00924 Bohr Magnetons or β_e). Shermaul *et al.* [61] as well as Brown and Plymate [21] were the first studies to converge at the 1% level (Brown and Plymate's value is $2.28(2)\times10^{-22}$ cm/molecule) after many prior determinations had discrepancies on the order of 10%. These values remain in close agreement with the (lower) values determined by CRDS ([14, 60]) and FTS+CRDS (this work). The precisions listed in Table 3 are indicative of data quality, but a cursory inspection of the variation from column to column quickly reveals how important *accuracy* is in these types of measurements. The accuracy of the intensity in our study is actually limited by uncertainty in the various pressure gauges (about $1–2.5\times10^{-3}$, or 0.1%–0.25%), indicating that the determined systematic offset (in comparison to HITRAN2012, based on [14]) of 0.5% remains statistically relevant.

The LBL parameters listed in Tables 4 and 5 and shown in Figs. 11 and 12 from this study closely resemble values determined by the prior CRDS studies [14, 16] which were used to update HITRAN in the HITRAN2012 edition [28]. Plots of the LBL parameters reveal smooth, systematic trends in both the values and the precision uncertainties. A comprehensive comparison to HITRAN2012 was performed as well as inspections of other parameters.

The foreign and self broadening parameters are shown in Figure 11c and 11d, respectively, units are cm^{-1}/atm (0.29587215 MHz/Pa). The air- and self-broadened widths from HITRAN2012 (as determined by Long *et al.* [14]) deviate by 3 to 15%. For both broadeners, the deviations at low *J* occur only for $P1P1$, $R1R1$ and $P3Q2$ and are roughly 8% or less. Agreement for the strongest transitions across both *P* and *R* is better than 3% until significant variability is observed in the fitted *R*-branch band head values. However, the variability in the band-head is not as pronounced and with the two outlier widths ($R21Q22$

and $R25R25$) are accidentally degenerate lines, producing a strong correlation between their lineshape parameters. The largest deviations all occur where LM is strongest but persist even when LM is set to zero. In the bandhead there is clearly some instability of the solution, and the width values are found to deviate further from the smooth trendline adopted in HITRAN2012 and Long *et al.* when assumptions about nearby transitions, or fixed values of these transitions are changed. These issues, primarily associated with pressure shifts and temperature dependences of pressure shifts, are discussed further below. Precisions on width values are generally on the order of 0.1%, comparable to the uncertainty due to accuracy of the pressure gauges and do not factor into the determinations of trends and correlations.

Foreign and self broadened widths have temperature dependences (n_X) that are parameterized with a power law expression in Eq. 7. HITRAN2012 utilized average values from multiple transitions as described by Brown and Plymate [21]. These unitless values are shown in Figures 12a and 12b along with the values determined for each transition in this study. The exponents from Brown and Plymate were deemed to have an accuracy of only ±15% (error bars in Figures 12a and 12b are based on precision), due to issues with controlling the cell temperature. In contrast, the precisions (error bars) from the present work are under 1% for most of the band. Based on maximum deviations, the accuracy of the power law exponent is only as good as the accuracy of the width measurement at a representative temperature, divided by the log of the ratio of temperature extrema (see Ref. [49] Eq. 4). The widths are certainly limited by the pressure gauge, which is, at worst, 0.25%. So a measurement range of 200–300 K gives, at best, 1.25% accuracy on the exponent. Since the width precisions range from 0.04–1.0%, we give 0.25% as a lower bound and 1.0% as an upper bound for the widths and derive a 1.25%–5% range for accuracies on the exponents. This improvement in accuracy allows a statistical comparison to Brown and Plymate, which are, on the average, 8% smaller (for air), with the strongest lines ($|m| = 8$) being 5,6,12, and 13% smaller for nitrogen, nitrogen, oxygen and oxygen; respectively. These strong lines are now estimated to have temperature exponent accuracies of 1.25%, such that a significant distinction between the parameter sets occurs. Sensitivity tests on the OCO-2 algorithm [62] indicate that the change in exponent equates to nearly 1 ppm change in the derived CO_2 fraction [62]. Based on the trend up to $J = 23$, values of the temperature exponents for $J > 23$ were held fixed to 0.63 for n_f and 0.75 for n_s.

The foreign and self pressure shifts (δ_X) are depicted in 11e and 11f and have units of cm^{-1}/atm (0.29587215 MHz/Pa). HITRAN2012 air pressure shift values are based on the polynomials provided by Long *et al.* [14], which are equivalent for both oxygen and air shift. Values for this polynomial are plotted along with the foreign pressure and self pressure shifts determined in this study. Values for the nitrogen pressure shift overlap at the strongest transitions, with the current values showing slightly less negative shifts at the center of the band and slightly more negative shifts at the highest quanta fitted, with values near the band head showing significant variability and increased uncertainties. Values for the oxygen pressure shift follow the same trend as for nitrogen, but are all offset to less negative values by 4×10^{-3} cm^{-1}/atm.

The temperature dependences of the pressure shift parameters (δ_x') are found to be significantly determinable and indicate that the pressure shifts become more negative at decreasing temperatures in the atmospheric temperature range. The values are depicted in 12c and 12d and have units of cm^{-1}/atm/K (0.29587215 MHz/Pa/K) with using the linear temperature dependence expression of Eq. 6. The temperature dependence of the nitrogen shift was found to start near zero at low J and increase monotonically throughout the determinable range, above $J = 23$ the parameters were fixed to a constant value of 5×10^{-5} $cm^{-1}atm^{-1}$ K^{-1}. For oxygen pressure shift temperature dependence the values initially rise at small J and then level off around 6×10^{-5} $cm^{-1}atm^{-1}$ K^{-1}, values up $J = 23$ were fixed to 3×10^{-5} $cm^{-1}atm^{-1}$ K^{-1}.

The unitless speed dependence parameters (S) are shown in Figure 12e. As expected the values are near 0.1 across the band as is typical for oxygen and nitrogen mixtures. Since speed-dependence is expected to be constant across a band and a trend towards slightly larger S values is observed on increasing J, attempts were made to also determine the heavily correlated motional (Dicke) narrowing. Long *et al.* [14] fitted Dicke narrowing, rather than speed-dependence, and trial fits were performed using either parameterization, as well as both simultaneously. Fitting both parameters produced divergent solutions. Fitting only one parameter at a time revealed that the CRDS data itself was unaffected by the choice, but that the FTS data had poorer residuals when fitted with Dicke narrowing alone. Certainly the intermediate pressure range of the FTS data, as well as unsaturated line centers, presents a stronger test for the effect. Finally, several tests were performed with speed-dependence fixed and Dicke narrowing optimized, these tests revealed poorer fits than with speed-dependence alone, and may be an indication that the algorithm in use for this case is not sufficiently accurate. Work is currently underway to integrate the Hartmann-Tran profile [52] into the program and these tests will then be repeated.

Line-mixing is often condensed to the line-by-line dependent dispersion coefficient, Y at a given temperature for tabulation and use in LBL codes (see Eqn. 9). Previously, Y factors from $-20 \leq m \leq 20$ were fitted at room temperature for both self-perturbed O_2 [12] and nitrogen perturbed O_2 [13] and these were used to guide Tran and Hartmann's empirical correction to their **W**-matrix [36]. In that study, all of the off-diagonal elements (odd and even ΔJs) were scaled between 0 and 1 with line-mixing for small quanta obtaining larger relative values and line-mixing for large quanta scaling to near zero, and J values around 10, near the room temperature P/R maxima, were scaled by $\sim\frac{1}{2}$. In Figure 12f the values from the present study (with no ΔJ odd elements and a constant empirical scaling of $\frac{1}{2}$) are compared to unscaled values from the full **W**-matrix provided by Ref. [22] as well as air values calculated from the experimentally determined room-temperature values reported by Predoi-Cross *et al.* [12, 13]. Several features evident in Figure 12f are worth noting (1) the bifurcation of the Y points between even and odd J, that was not observed in fitted Y-values of Refs. [12, 13] disappears entirely upon removal of the odd ΔJ matrix elements; (2) the J dependences of the curves are all of correct sign and cross through each other at the strongest portions of the sub-bands; (3) the empirical factor of $\frac{1}{2}$ applied in the present study tracks well with fitted values [12, 13] where they are available. The need for J-dependent empirical scaling in Ref. [36] was deemed to be a consequence of the assumptions about

case *a* intensities in the matrix element scale factors, however these errors are largely of just a few %, and the empirical corrections amount to 0–100% scaling, which also significantly reduced couplings in the band-head region where many lines are accidentally degenerate. The removal of odd ΔJ elements in this work accomplishes significant reductions of couplings in the band-head region and allows a scalar to accommodate matching of the LM model. Implementation of the full **W**-matrix, without *J*-dependent empirical scaling, retains a strong link to the fundamental collisional theory and provides for a well-defined temperature dependent model of the LM. These modified matrices, as well as Y values determined for air at a variety of temperatures, are provided in the supplemental material.

5.1. Testing in OCO-2 Level 2 Algorithm

A multi-dimensional table containing the various cross-sections of O_2 A-band absorption with the dependent variables of temperature, air pressure and water pressure is produced using the results of the fitting to laboratory and atmospheric data. The table incorporates both resonant and non-resonant absorption as well as the interfering species H_2O which is also allowed to be a foreign broadener [26]. It is generated using the physical model portion of the multispectral fitting program as part of the compiled code. The resulting table is one of the absorption coefficient (ABSCO) tables that are primary inputs to the ACOS (Level 2) Algorithm [5]. At the time of preparing and testing this table, the OCO-2 mission has acquired more than one-year of data on orbit and subsets of the data analyzed using the seventh version of the Level 2 code (v7.1, which uses ABSCO table v4.2) were identified for diverse atmospheric conditions, minimal aerosol loading, and cloud-free observations.

To compare and test the new ABSCO table several physically relevant aspects of the level-2 products are tracked including the averaged spectral residuals, surface pressure and impact on aerosol retrieval. Since a set of empirically generated equivalent orthogonal functions (EOFs) are introduced to remove persistent spectral residuals in v7.1, a special processing of this version of the algorithm, in which no EOFs are applied, was run to enable the spectral residuals to be ‘true’ and directly comparable to tests with the new spectral data.

The results of the testing are somewhat mixed: 1) there is a clear improvement in the dependence of the derived surface pressure as compared to ground truth measurements; 2) the airmass dependence of the derived surface pressure is strongly reduced; 3) persistent and slowly varying spectral residual features extending across the *P* and *R* branches disappeared, but new sharp, localized features appeared between the spin-doublets; 4) aerosol loading (at the small values selected for these tests) is not noticeably affected. These results are encouraging, indicating that the airmass dependence of the derived surface pressure had been linked to an imbalance between the effects of LM and CIA, which are carefully balanced as well as possible in the new ABSCO table. The spectral residual changes reflect the band-wide change in intensity that has resulted from this new balance, which has effectively made the central regions of the *P, R* branches stronger at high pressure, and reduced the amount of absorption in the high *J*, *P*-branch. The residuals near the band-head are different, and the abrupt transition from resonant to non-resonant absorption in this area is actually slightly worse than the prior ABSCO table (v4.2). The most disconcerting result of the test is the appearance of regular residuals between the spin doublets. These features

are also discernable in the CRDS *P*-branch data, and further modeling of the ΔJ odd LM interactions has been shown to reduce these features, but there is not currently enough information in the data sets described here to reliably balance this additional (and weaker) LM with the CIA. Overall the change in residuals is a net reduction (in the root-mean-square), and an *ad hoc* scaling parameter that was previously necessary to minimize surface pressure bias in ABSCO v4.2 is now unnecessary. The remaining spectral residuals will likely be treated with new EOFs in future level 2 processing.

6. Conclusion

This work represents the first concerted effort to treat O_2 LM, CIA and non-Voigt lineshapes on temperature dependent laboratory data. The multispectral fitting program was modified as necessary to accommodate the combination of FTS and CRDS data, as well as to incorporate approximate CIA while determining LBL and adjusting LM. Complementary data from both FTS and CRDS in the *P*-branch improved atmospheric models directly, while atmospheric datasets were essential to proper tuning of the LM and CIA in the *R*-branch. Besides a scale factor of 1/2 on the LM, the LM in the *R*-branch closely resembles that of Tran *et al.* [22] with the absence of coupling between sub-bands. LBL parameters closely resemble those of HI-TRAN2012 and its data sources. Together the derived LBL, LM and CIA provide a self-consistent parameter set, traceable to calibrated lab and atmospheric data, for the production of new ABSCO tables. The use of an improved ABSCO table in the retrieval of atmospheric trace gas concentrations reduces band-wide residuals in the spectral data and reduces biases of the surface pressure associated with systematic errors in previous spectroscopic data sources. The ABSCO table from this work (version 5.0) is available upon request along with those associated with CO_2 absorption. An update to LBLRTM [63] that incorporates the results of this work will also be available.

This effort has reduced biases and improved retrievals of atmospheric data, however, it is clear that some LM/CIA issues remain in the high density models. Efforts are currently underway to record reduced temperature CRDS data in this spectral region, including the *R*-branch, and a photo-acoustic spectrometer at California Institute of Technology [64] has been refitted for low-temperature measurements as well. The expected datasets will provide much needed data at high density for both long (CRDS) and short (PAS) pathlengths.

Supplementary Material

Refer to Web version on PubMed Central for supplementary material.

Acknowledgments

Portions of the research described in this paper were performed at the Jet Propulsion Laboratory, California Institute of Technology, under contract with the National Aeronautics and Space Administration. Copyright 2016 California Institute of Technology. Government sponsorship acknowledged. Research performed at the College of William and Mary was supported by a Grant from the Jet Propulsion Laboratory, California Institute of Technology. The authors gratefully acknowledge financial support from the U.S. Department of Energy, Office of Science, Office of Biological and Environmental Research, Environmental Sciences Division, as part of the ARM programme under grant DE-FG02-90ER610. Support was also provided by the National Institute of Standards and Technology (NIST) Greenhouse Gas Measurements and Climate Research Program and the Orbiting Carbon Observatory (OCO) project, a National Aeronautics and Space Administration (NASA) Earth System Science Pathfinder (ESSP) mission. Manufacturers and product names are listed solely for completeness. These specific citations neither

constitute an endorsement of the products nor imply that similar products from other companies would be less suitable. We thank Dr. Ha Tran for providing line mixing coefficients for pure O_2. We also thank Dr. Debra Wunch for providing TCCON spectra and guidance on good days for use on our analysis.

References

1. Rothman LS, Barbe A, Benner DC, Brown LR, Camy-Peyret C, Carleer MR, et al. The HITRAN Molecular Spectroscopic Database: Edition Of 2000 Including Updates Through 2001. J Quant Spectrosc Radiat Transfer. 2003; 82(1):5–44.
2. Rothman LS, Jacquemart D, Barbe A, Benner DC, Birk M, Brown LR, et al. The HITRAN 2004 Molecular Spectroscopic Database. J Quant Spectrosc Radiat Transfer. 2005; 96(2):139–204.
3. Rothman LS, Gordon IE, Barbe A, Benner DC, Bernath PE, Birk M, et al. The HITRAN 2008 Molecular Spectroscopic Database. J Quant Spectrosc Radiat Transfer. 2009; 110(9–10):533–572.
4. Eldering A, Boland S, Solish B, Crisp D, Kahn P, Gunson M. High Precision Atmospheric CO_2 Measurements From Space: The Design And Implementation Of OCO-2. Aerospace Conference, 2012 IEEE. 2012:1–10.
5. O'Dell C, Connor B, Bösch H, O'Brien D, Frankenberg C, Castano R, et al. The ACOS CO_2 Retrieval Algorithm Part 1: Description and Validation Against Synthetic Observations. Atmos Meas Tech Discuss. 2011; 4(5):6097–6158. DOI: 10.5194/amtd-4-6097-2011
6. O'Dell CW, Connor B, Bösch H, O'Brien D, Frankenberg C, Castano R, et al. The ACOS CO_2 Retrieval Algorithm - Part 1: Description And Validation Against Synthetic Observations. Atmos Meas Tech. 2012; 5(1):99–121. DOI: 10.5194/amt-5-99-2012
7. Crisp D, Fisher BM, O'Dell C, Frankenberg C, Basilio R, Bösch H, et al. The ACOS CO_2 Retrieval Algorithm - Part II: Global X-CO_2 Data Characterization. Atmos Meas Tech. 2012; 5(4):687–707. DOI: 10.5194/amt-5-687-2012
8. Crisp, D.; Bösch, H.; Brown, LR.; Castano, R.; Christi, M.; Connor, B., et al. Tech Rep OCO D-65488. NASA Jet Propulsion Laboratory, California Institute of Technology; Pasadena, CA: OCO (Orbiting Carbon Observatory)-2 Level 2 Full Physics Retrieval Algorithm Theoretical Basis. version 1.0 Rev 4, http://disc.sci.gsfc.nasa.gov/acdisc/documentation/OCO-2L2FPATBDv1rev4Nov10.pdf [last access: January 2012]
9. Thompson DR, Chris Benner D, Brown LR, Crisp D, Malathy Devi V, Jiang Y, et al. Atmospheric Validation of High Accuracy CO_2 Absorption Coefficients for the OCO-2 Mission. J Quant Spectrosc Radiat Transfer. 2012; 113(17):2265–2276. http://dx.doi.org/10.1016/j.jqsrt.2012.05.021.
10. Kuze A, Suto H, Nakajima M, Hamazaki T. Thermal And Near Infrared Sensor For Carbon Observation Fourier-Transform Spectrometer On The Greenhouse Gases Observing Satellite For Greenhouse Gases Monitoring. Appl Opt. 2009; 48(35):6716–6733. [PubMed: 20011012]
11. Wunch D, Toon GC, Wennberg PO, Wofsy SC, Stephens BB, Fischer ML, et al. Calibration Of The Total Carbon Column Observing Network Using Aircraft Profile Data. Atmos Meas Tech. 2010; 3(5):1351–1362.
12. Predoi-Cross A, Hambrook K, Keller R, Povey C, Schofield I, Hurtmans D, Over H, Mellau GC. Spectroscopic Lineshape Study of the Self-Perturbed Oxygen A-Band. J Mol Spectrosc. 2008; 248:85–110.
13. Predoi-Cross A, Holladay C, Heung H, Bouanich J-P, Mellau GC, Keller R, Hurtmans DR. Nitrogen-Broadened Lineshapes in the Oxygen A-Band: Experimental Results and Theoretical Calculations. J Mol Spectrosc. 2008; 251:159–175.
14. Long DA, Havey DK, Okumura M, Miller CE, Hodges JT. O_2 A-Band Line Parameters To Support Atmospheric Remote Sensing. J Quant Spectrosc Radiat Transfer. 2010; 111(14):2021–2036. DOI: 10.1016/j.jqsrt.2010.05.011
15. Robichaud DJ, Hodges JT, Brown LR, Lisak D, Masłowski P, Yeung LY, et al. Experimental Intensity and Lineshape Parameters of the Oxygen A-Band using Frequency-Stabilized Cavity Ring-Down Spectroscopy. J Mol Spectrosc. 2008; 248(1):1– 13. DOI: 10.1016/j.jms.2007.10.010
16. Long DA, Havey DK, Yu SS, Okumura M, Miller CE, Hodges JT. O_2 A-Band Line Parameters To Support Atmospheric Remote Sensing. Part II: The Rare Isotopologues. J Quant Spectrosc Radiat Transfer. 2011; 112(16):2527–2541. DOI: 10.1016/j.jqsrt.2011.07.002

17. Robichaud DJ, Hodges JT, Lisak D, Miller CE, Okumura M. High-Precision Pressure Shifting Measurement Technique Using Frequency-Stabilized Cavity Ring-Down Spectroscopy. J Quant Spectrosc Radiat Transfer. 2008; 109(3):435–444.
18. Long DA, Havey DK, Okumura M, Pickett HM, Miller CE, Hodges JT. Laboratory Measurements And Theoretical Calculations Of O_2 A-Band Electric Quadrupole Transitions. Phys Rev A. 2009; 80(4):12.doi: 10.1103/PhysRevA.80.042513
19. Havey DK, Long DA, Okumura M, Miller CE, Hodges JT. Ultra-Sensitive Optical Measurements Of High-J Transitions in the O_2 A-Band. Chem Phys Lett. 2009; 483(1–3):49–54. DOI: 10.1016/j.cplett.2009.10.067
20. Lisak D, Maslowski P, Cygan A, Bielska K, Wojtewicz S, Piwinski M, et al. Line Shapes and Intensities of Self-Broadened O2b ∑1g+(ν=1)←X ∑3v-(ν=0) Band Transitions Measured By Cavity Ring-Down Spectroscopy. Phys Rev A. 2010; 81(4):10.doi: 10.1103/PhysRevA.81.042504
21. Brown LR, Plymate C. Experimental Line Parameters Of The Oxygen A-Band At 760 nm. J Mol Spectrosc. 2000; 199(2):166–179. [PubMed: 10637102]
22. Tran H, Boulet C, Hartmann JM. Line Mixing And Collision-Induced Absorption By Oxygen In The A-Band: Laboratory Measurements, Model, And Tools For Atmospheric Spectra Computations. J Geophys Res D: Atmos. 111(D15)
23. Long DA, Robichaud DJ, Hodges JT. Frequency-Stabilized Cavity Ring-Down Spectroscopy Measurements Of Line Mixing And Collision-Induced Absorption In The O_2 A-Band. J Chem Phys. 2012; 137(1):014307.doi: 10.1063/1.4731290 [PubMed: 22779648]
24. Vess E, Wallace C, Campbell H, Awadalla V, Hodges J, Long D, et al. Measurement Of H_2O Broadening Of O_2 A-Band Transitions And Implications For Atmospheric Remote Sensing. J Phys Chem A. 2012; 116(16):4069–4073. [PubMed: 22452330]
25. Fanjoux G, Millot G, Saint-Loup R, Chaux R, RL. Coherent anti-Stokes Raman spectroscopy study of collisional broadening in the O_2-H_2O Q branch. J Chem Phys. 1994; 101:1061–1071.
26. Drouin BJ, Payne V, Oyafuso F, Sung K, Mlawer E. Pressure Broadening of Oxygen by Water. J Quant Spectrosc Radiat Transfer. 2014; 133:190–198.
27. Golubiatnikov GY, Koshelev MA, Krupnov AF. Reinvestigation Of Pressure Broadening Parameters At 60-GHz Band And Single 118.75 GHz Oxygen Lines At Room Temperature. J Mol Spectrosc. 2003; 222(2):191–197. DOI: 10.1016/j.jms.2003.08.002
28. Rothman LS, Gordon IE, Babikov Y, Barbe A, Chris Benner D, Bernath PF, et al. The HITRAN 2012 Molecular Spectroscopic Database. J Quant Spectrosc Radiat Transfer. 2013; 130(0):4–50. DOI: 10.1016/j.jqsrt.2013.07.002
29. Spiering FR, Kiseleva MB, Filippov NN, Naus H, van Lieshout B, Weijenborg C, et al. Line Mixing And Collision Induced Absorption In The Oxygen A-Band Using Cavity Ring-Down Spectroscopy. The J Chem Phys. 2010; 133(11):114305. [PubMed: 20866137]
30. Long DA, Hodges JT. On Spectroscopic Models Of The O_2 A-Band And Their Impact Upon Atmospheric Retrievals. J Geophys Res D: Atmos. 117(D12)
31. Moazzen-Ahmadi N, Oliaee JN, Ozier I, Wishnow E, Sung K, Crawford T, et al. An Intensity Study Of The Torsional Bands Of Ethane At 35 m. J Quant Spectrosc Radiat Transfer. 2015; 151:123–132.
32. Wishnow E, Leung A, Gush H. Cryogenic Multiple Reflection Absorption Cell And Fourier Transform Spectrometer System For The Far Infrared. Rev Sci Instrum. 1999; 70(1):23–31.
33. Turner DD, Clough SA, Lijegren JC, Clothiaux EE, Cady-Pereira KE, Gaustad KL. Retrieving Liquid Water Path And Precipitable Water Vapor From The Atmospheric Radiation Measurement (ARM) Microwave Radiometers. IEEE Trans Geosci Remote Sens. 2007; 45(11):3680–3690. DOI: 10.1109/tgrs.2007.903703
34. Benner DC, Rinsland CP, Devi VM, Smith MAH, Atkins D. A Multispectrum Nonlinear Least-Squares Fitting Technique. J Quant Spectrosc Radiat Transfer. 1995; 53:705–21.
35. Falke S, Tiemann E, Lisdat C, Schnatz H, Grosche G. Transition Frequencies Of The D Lines Of ^{39}K, ^{40}K, And ^{41}K Measured With A Femtosecond Laser Frequency Comb. Phys Rev A. 2006; 74(3):9.doi: 10.1103/PhysRevA.74.032503
36. Tran H, Hartmann JM. An improved O-2 A-Band Absorption Model and its Consequences for Retrievals of Photon Paths and Surface Pressures. J Geophys Res D: Atmos. 113(D18)

37. DePristo AE, Augustin SD, Ramaswamy R, Rabitz H. Quantum Number and Energy Scaling for Nonreactive Collisions. The Journal of Chemical Physics. 1979; 71(2):850–865.
38. Niro F, Boulet C, Hartmann J. Spectra calculations in central and wing regions of CO_2 IR bands between 10 and 20 μm. I: model and laboratory measurements. J Quant Spectrosc & Radiat Trans. 2004; 88(4):483–498. DOI: 10.1016/j.jqsrt.2004.04.003
39. Rosenkranz PW. Shape of 5 mm Oxygen Band in Atmosphere. IEEE Trans Antennas Propag. 1975; AP23(4):498–506.
40. Yu SS, Drouin BJ, Miller CE. High Resolution Spectral Analysis Of Oxygen IV. Energy Levels, Partition Sums, Band Constants, RKR Potentials, Franck-Condon Factors Involving The X ∑3g-, a $^1\Delta_g$, and b ∑1g+ States. J Chem Phys. 2014; 141(17):12.doi: 10.1063/1.4900510
41. Yu SS, Miller CE, Drouin BJ, Muller HSP. High Resolution Spectral Analysis Of Oxygen I. Isotopically Invariant Dunham Fit For The X ∑3g-, a $^1\Delta_g$, b ∑1g+ States. J Chem Phys. 2012; 137(2):20.doi: 10.1063/1.4719170
42. Drouin BJ, Gupta H, Yu S, Miller CE, Muller HSP. High Resolution Spectral Analysis of Oxygen. II. Rotational Spectra of $a^1\Delta_g$ O_2 Isotopologues. J Chem Phys. 2012; 137(2):11.doi: 10.1063/1.4719169
43. Drouin BJ, Yu S, Elliott BM, Crawford TJ, Miller CE. High Resolution Spectral Analysis of Oxygen. III Laboratory Investigation of the Airglow Bands. J Chem Phys. 2013; 139(14):11.doi: 10.1063/1.4821759
44. Watson J. Rotational Line Intensities in $^3\Sigma$-$^1\Sigma$ Electronic Transitions. Can J Phys. 1968; 46(14): 1637.
45. Herman R, Wallis RF. Influence of Vibration-Rotation Interaction on Line Intensities in Vibration-Rotation Bands of Diatomic Molecules. The J Chem Phys. 1955; 23(4):637–646.
46. Pine AS, Looney JP. N_2 and Air Broadening in the Fundamental Bands of HF and HCl. J Mol Spectrosc. 1987; 122:41–55.
47. Ciurylo R. Shapes of Pressure- and Doppler- Broadened Spectral Lines in the Core and Near Wings. Phys Rev A. 1998; 58:1029–1039.
48. Rohart F, Mäder H, Nicolaisen HW. Speed Dependence of Rotational Relaxation Induced by Foreign Gas Collisions: Studies of CH_3F by Millimeter Wave Coherent Transients. J Chem Phys. 1994; 101:6475–6488.
49. Priem D, Rohart F, Colmont JM, Wlodarczak G, Bouanich JP. Lineshape study of the $J = 3 \leftarrow 2$ rotational transition of CO perturbed by N_2 and O_2. J Mol Struct. 2000; 517–518:435–454.
50. Letchworth KL, Benner DC. Rapid And Accurate Calculation Of The Voigt Function. J Quant Spectrosc Radiat Transfer. 2007; 107(1):173–192.
51. Rothman LS, Gordon IE, et al. HITRANonline. J Quant Spectrosc Radiat Transfer.
52. Tran H, Ngo NH, Hartmann JM. Efficient Computation of Some Speed-Dependent Isolated Line Profiles. J Quant Spectrosc Radiat Transfer. 2013; 129:199–203. DOI: 10.1016/j.jqsrt.2013.06.015
53. Hartmann, JM.; Boulet, C.; Robert, D. Collisional Effects On Molecular Spectra. 1. Elsevier; Amsterdam: 2008.
54. Lévy, A.; Lacome, N.; Chackerian, C. Collisional Line Mixing in Spectroscopy of the Earths Atmosphere and Interstellar medium. Narahari Rao, K.; Weber, A., editors. Academic Press; Boston, MA: 1992.
55. Lewis GN. The Magnetism of Oxygen and the Molecule O_4. J Am Chem Soc. 1924; 46(9):2027–2032.
56. Maté B, Lugez C, Fraser GT, Lafferty WJ. Absolute Intensities for the O_2 1.27 μm Continuum Absorption. J Geophys Res. 1999; 104:30,585.
57. Alvarado MJ, Payne VH, Mlawer EJ, Uymin G, Shephard MW, Cady-Pereira KE, et al. Performance of the Line-By-Line Radiative Transfer Model (LBLRTM) for Temperature, Water Vapor, and Trace Gas Retrievals: Recent Updates Evaluated with IASI Case Studies. Atmos Chem Phys. 2013; 13(14):6687–6711. DOI: 10.5194/acp-13-6687-2013
58. Spiering FR, Kiseleva MB, Filippov NN, van Lieshout B, van der Veen AMH, van der Zande WJ. The Effect Of Collisions With Nitrogen On Absorption By Oxygen In The A-Band Using Cavity Ring-Down Spectroscopy. Mol Phys. 2011; 109(4):535–542. DOI: 10.1080/00268976.2010.533709

59. Lique F. Temperature Dependence of the Fine-Structure Resolved Rate Coefficients for collisions of O2(X ∑3g-) with He. J Chem Phys. 132(4)
60. Long DA, Havey DK, Okumura M, Pickett HM, Miller CE, Hodges JT. Laboratory Measurements and Theoretical Calculations of O_2 A-Band Electric Quadrupole Transitions. Phys Rev A. 2009; 80:042513.
61. Schermaul R, Learner RCM. Precise Line Parameters and Transition Probability of the Atmospheric A Band of Molecular Oxygen $^{16}O_2$. J Quant Spectrosc Radiat Transfer. 1999; 61:781–794.
62. Connor, B. Personal Communication. 2015.
63. Clough SA, Shephard MW, Mlawer EJ, Delamere JS, Iacono MJ, Cady-Pereira K, Boukabara S, Brown PD. Atmospheric radiative transfer modeling: a summary of the AER codes. J Quant Spectrosc Radiat Transfer. 2005; 91:233–244.
64. Bui, T. Ph D Thesis. California Institute of Technology; Cavity-enhanced spectroscopies for applications of remote sensing, chemical kinetics and detection of radical species.
65. Pickett HM. The Fitting And Prediction Of Vibration-Rotation Spectra With Spin Interactions. J Mol Spectrosc. 1991; 148(2):371–377.
66. Safronova UI, Safronova MS. High-Accuracy Calculation Of Energies, Lifetimes, Hyperfine Constants, Multipole Polarizabilities, And Blackbody Radiation Shift in ^{39}K. Phys Rev A. 2008; 78(5):052504.
67. de Laeter JR, Böhlke JK, De Biévre P, Hidaka H, Peiser H, Rosman K, et al. Atomic Weights Of The Elements. Review 2000 (IUPAC Technical Report). Pure Appl Chem. 2003; 75(6):683–800.
68. Audi G, Wapstra AH, TC. The 2003 Mass Evaluation: (II). Tables, Graphs and References. Nuc Phys A. 2003; 729(1):337–676.

1. Highlights

1. Comprehensive study of resonant and non-resonant oxygen absorption in the NIR.
2. Multispectrum analysis combining Fourier Transform and Cavity Ringdown Spectra
3. Speed dependence of lineshape determined.
4. Temperature dependences of lineshape parameters obtained.
5. Modified models for collision induced absorption and collisional relaxation

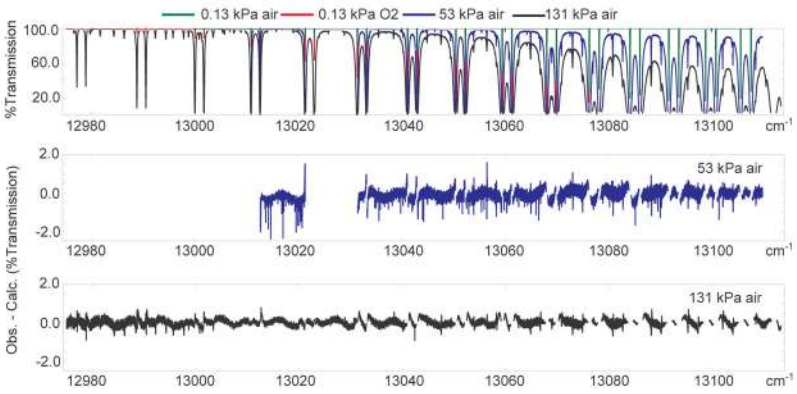

Figure 1.

Cavity Ring Down Spectra included in the multispectrum analysis. Pure and air ('NIST standard') were used. Four spectra at room temperature are plotted below: 0.133 kPa (1 Torr) O_2 (red trace) and three ('NIST standard') air at 0.133, 53.3, 133.3 kPa (1,400,1000 Torr) in green, blue and black, respectively. Lower panels indicate residuals from the presented analysis, a few segments of the 53.3 kPa (400 Torr) air spectrum were removed from the analysis due to an unresolved calibration issue.

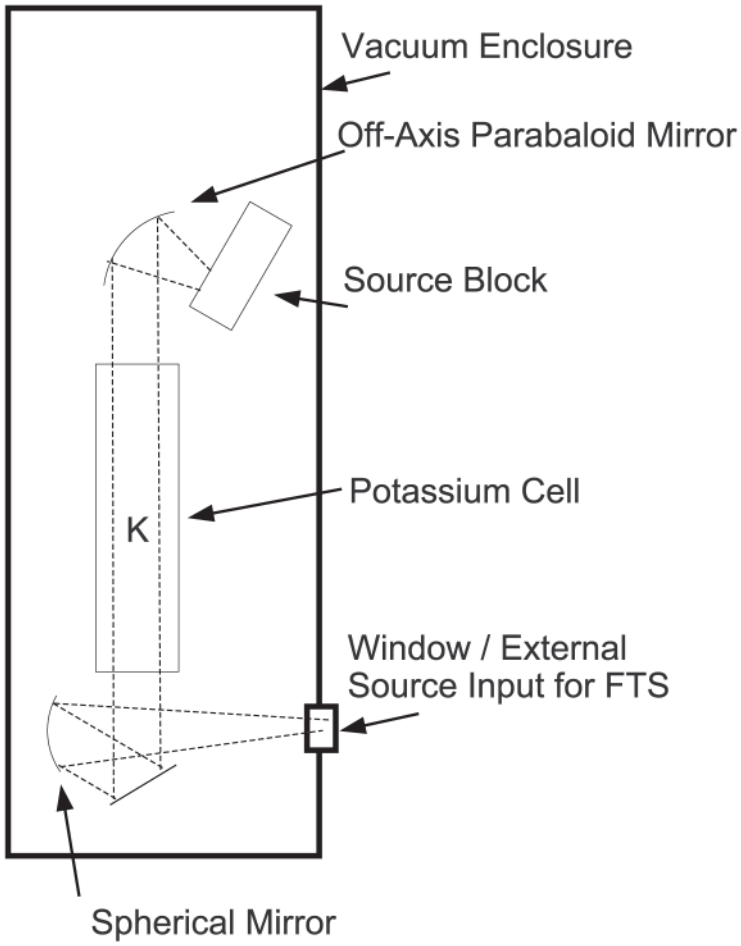

Figure 2.

Schematic diagram of external source chamber containing calibration gas cell and 100W Tungsten filament bulb. Optics are standard items from Newport and are aligned with positioning stages prior to evacuation. The rest of the FTS was configured as in Ref. [31]

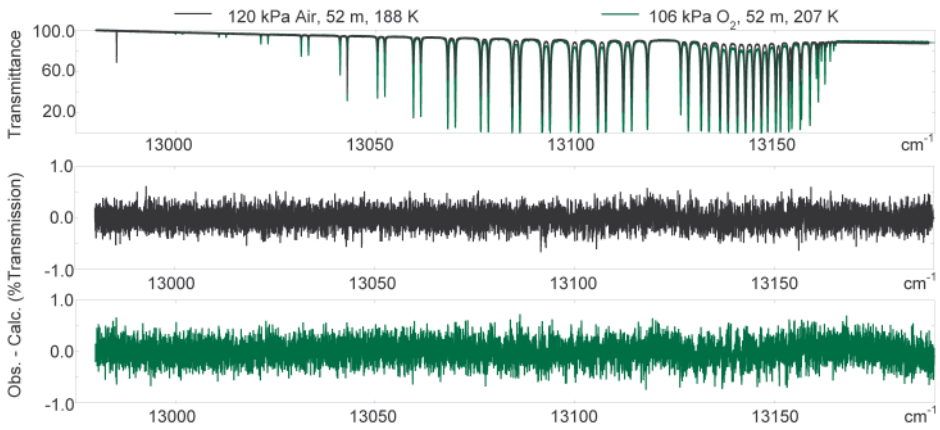

Figure 3.

(top) Typical Fourier Transform spectra of air (black) and pure O_2 (green) included in the multispectrum analysis. The pathlength is 52.00(5) m, the sample pressures are 120 kPa (899 Torr) air and 106 kPa (794 Torr) O_2, and the cell temperatures are 187.9(4) K and 206.8(6) K, respectively. (bottom panels) residuals from analysis of the 22 spectra listed in Table 1 described in text.

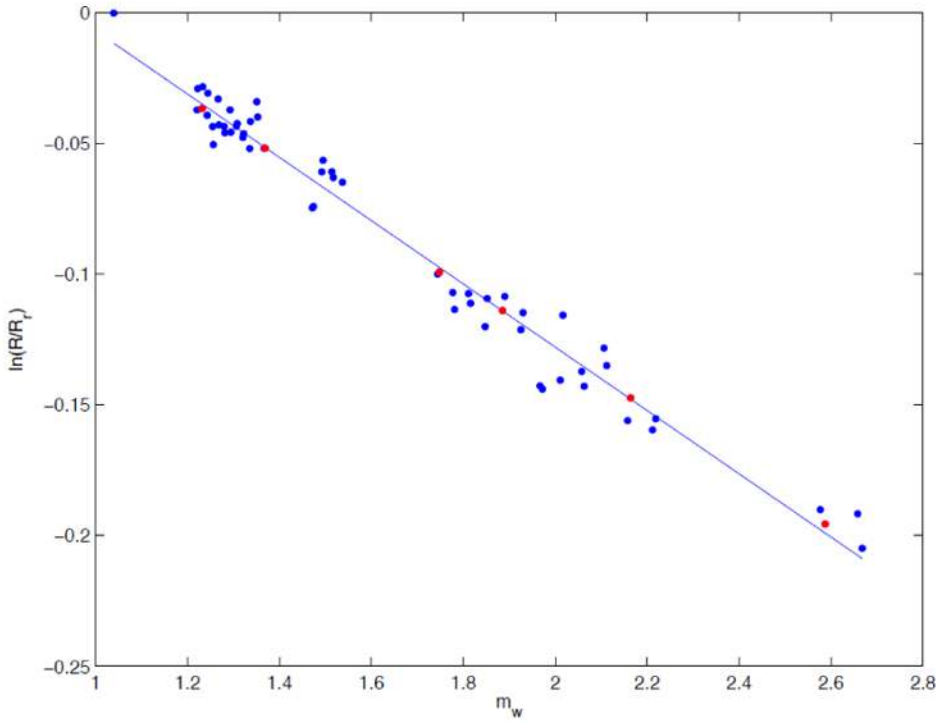

Figure 4.

Logarithm of the scaled irradiances (blue dots) (actually ln[R(11532)/R_{ref}(11532)]) for July 18, 2012 (1836-2348 UT) plotted *vs.* water vapor airmass factor, m_w, and the least-squares fitted line (blue). Also shown (red dots) are the values resulting from the sub-sampling procedure described in the text.

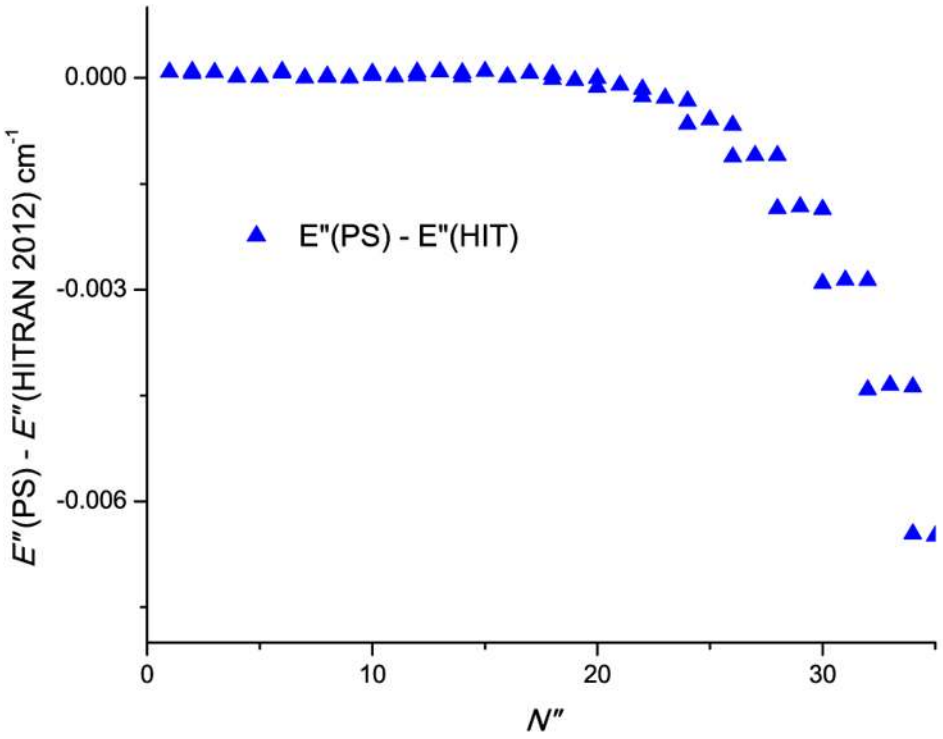

Figure 5.

Difference between lower state energies of Yu *et al.* [40] and HITRAN2012 [28], plotted *vs.* the quantum number N'' where $J'' = N'' + S''$.

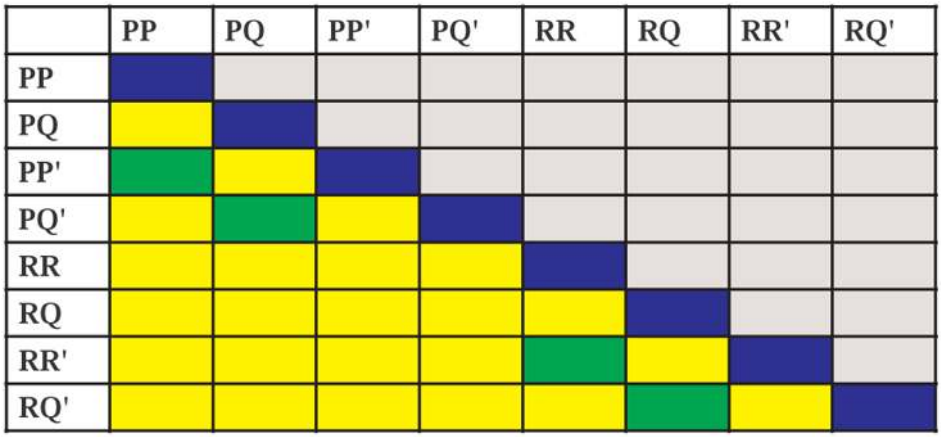

Figure 6.

Schematic representation of the line mixing collisional relaxation **W** matrix. Rows and columns each represent a given transition, which may occur in one of four sub- bands according to $^3\Sigma - {}^1\Sigma$ selection rules, primes indicate a different transition within a given sub-band. Diagonal values (blue) are collisional parameters for a given transition per Eqs. 6 and 7. Off-diagonal values are taken from theory [22, 36] and incorporated into the data fitting program. Only the lower triangle (yellow and green) are input since the upper triangle (grey squares) is calculated by detailed balance within the program. Inclusion of all yellow (extra-subband) and green (intra-subband) elements results in substantial fitting residuals, but exclusion of the yellow (extra-subband) elements provides an acceptable solution.

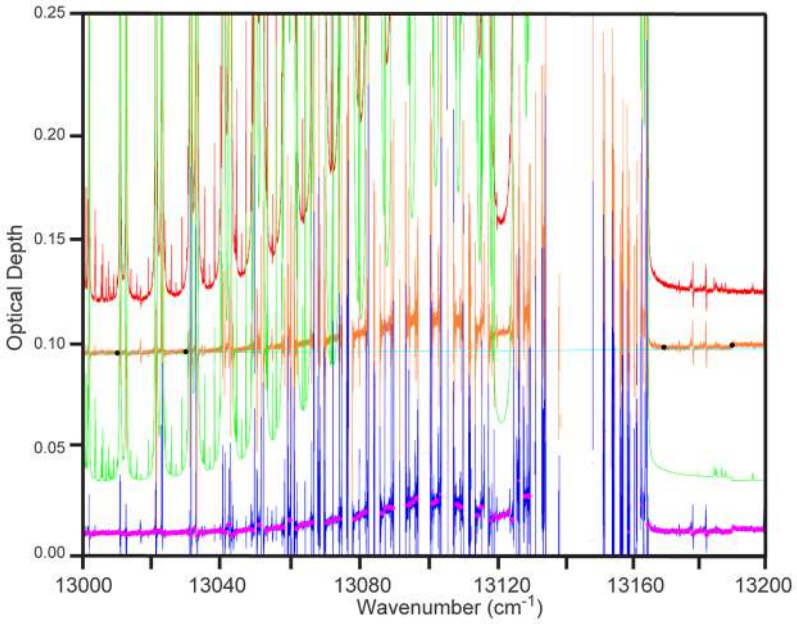

Figure 7.

Optical depths derived from TCCON FTS spectra (red), sum of O_2 LBL+LM and LBLRTM optical depths (green), difference of TCCON FTS and O_2 LBL+LM and LBLRTM optical depths (orange), aerosol optical depths (cyan) unknown optical depths (blue) and unknown optical depths filtered in 1 cm^{-1} bins (magenta, see text for description of filtering method)) for one of the cases analyzed in this study (July 18th, 2012, 4/69–2348 UT).

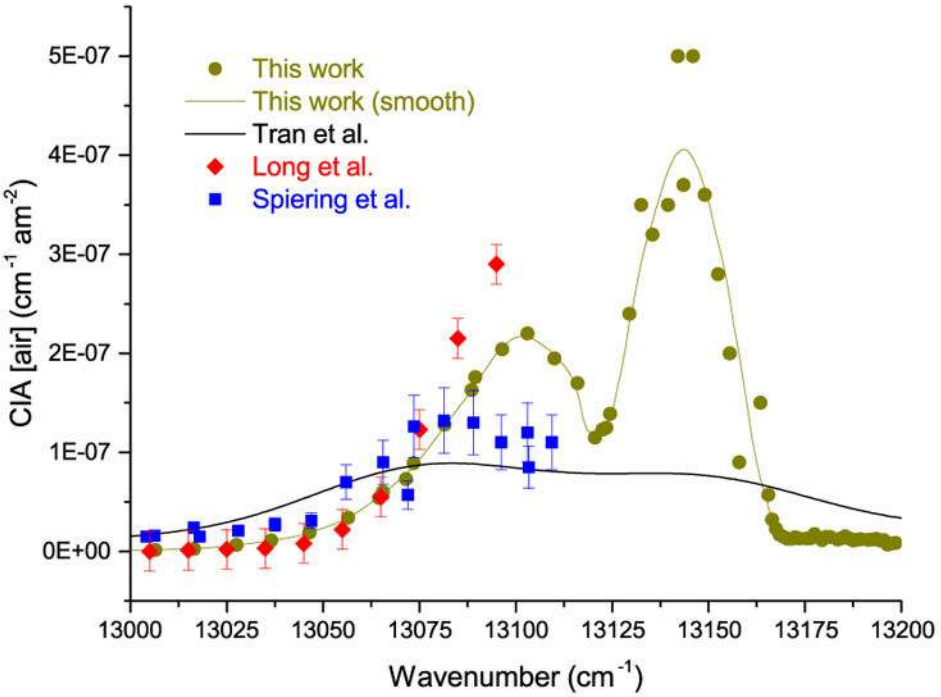

Figure 8.

Comparison with Long et al. 2012 [23] (red) and Spiering et al. 2011 [58] (blue) and present study (green) collision induced absorption coefficients for air ($\varrho_{O_2} = 0.21$, ($\varrho_{N_2} = 0.79$). One amagat (am) is the density of gas at 101325 Pa and 273.15 K.

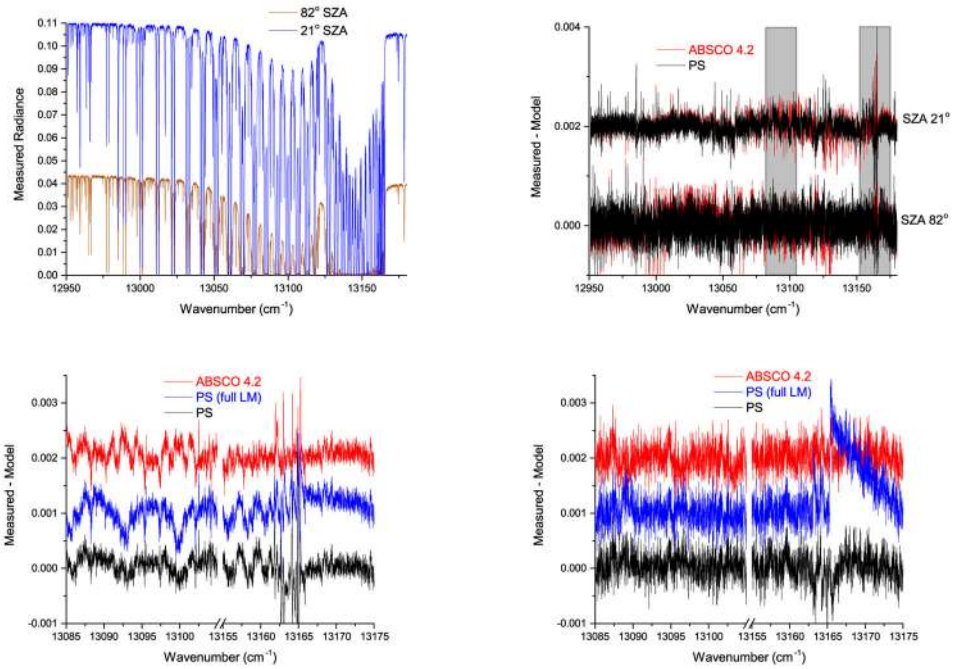

Figure 9.

[top left] Selected atmospheric TCCON spectra used to validate results from July 18th, 2012 at solar zenith angles of 21° (brown) and 82° (blue). [top right] Residuals from prior work (ABSCO 4.2 in red) and present study (PS black) across the A-band, the 21° solar zenith angle residuals are offset and scaled by the background radiance ratio (40%) for clarity. Expanded views of residuals in P-branch maximum and R-branch band-head regions are given at solar zenith angle 21° [bottom left] and 82° [bottom right]. The bottom panels depict residuals from prior work (ABSCO 4.2 in red), a rejected analysis incorporating all of the line-mixing parameters from theory (PS (full LM) blue), the analysis presented in this work (PS - black). Spectral radiances are in photons/s/m^2/sr/cm^{-1}, but with arbitrary scaling.

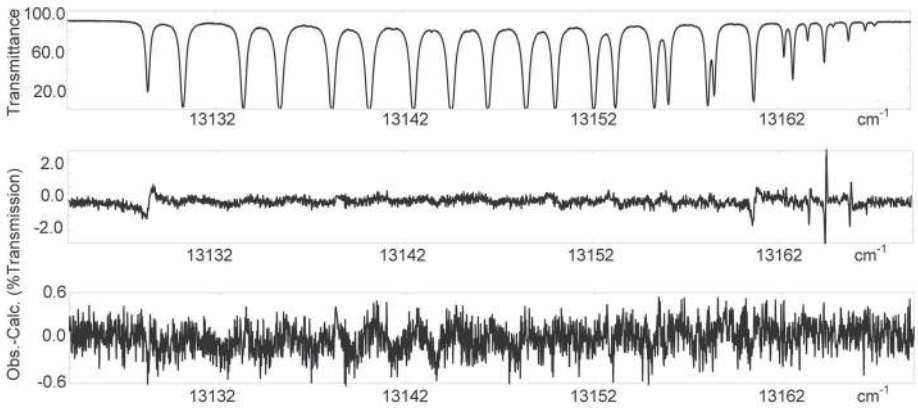

Figure 10.

(top) R-branch portion of FTS data scan with pathlength 52.00(5) m, sample pressure 106 kPa (794 Torr) pure O_2 and cell temperature −66.35°C. (middle) Residuals following LBL optimization with full LM (scaled by 1/2) included. (lower) Residuals following LBL optimization with odd ΔJ LM removed (sub-branch mixing only).

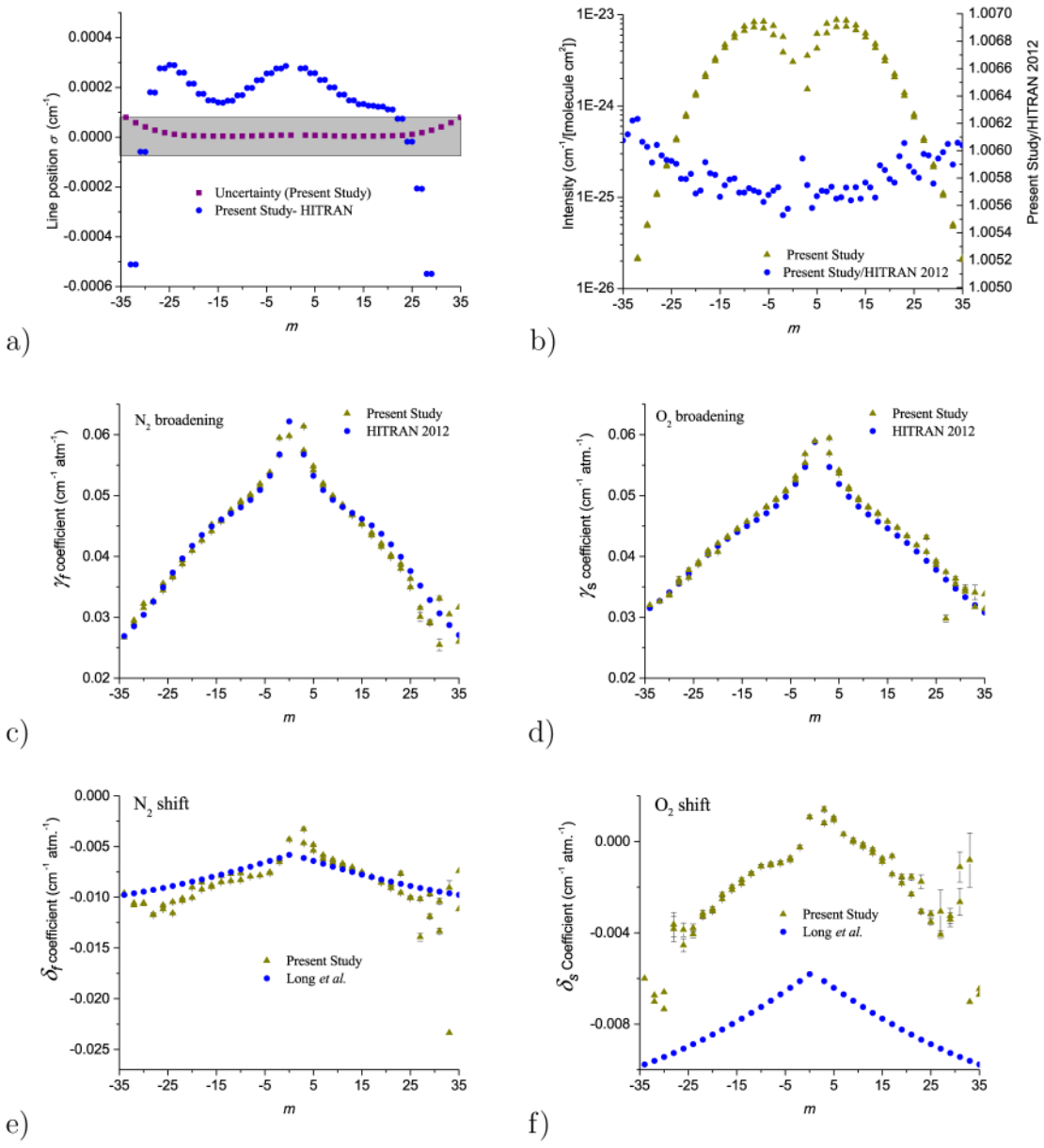

Figure 11.

Least squares fitted and fixed values in the LBL for oxygen A-band. (a) position differences (this work - HITRAN2012) [blue], uncertainties in positions [purple], shaded box indicates CRDS accuracy, the FTS accuracy encompasses the chart (b) intensity values at 296 K [green] and ratios to HITRAN2012 [blue] (c) nitrogen broadened halfwidth coefficients, this work [green], (derived from) HITRAN2012 [blue] (d) oxygen broadened halfwidth coefficients, this work [green], HITRAN2012 [blue] (e) nitrogen pressure shift coefficients, this work [green], Long *et al.* [14] [blue] (f) oxygen pressure shift coefficients, this work [green], Long *et al.* [14] [blue].

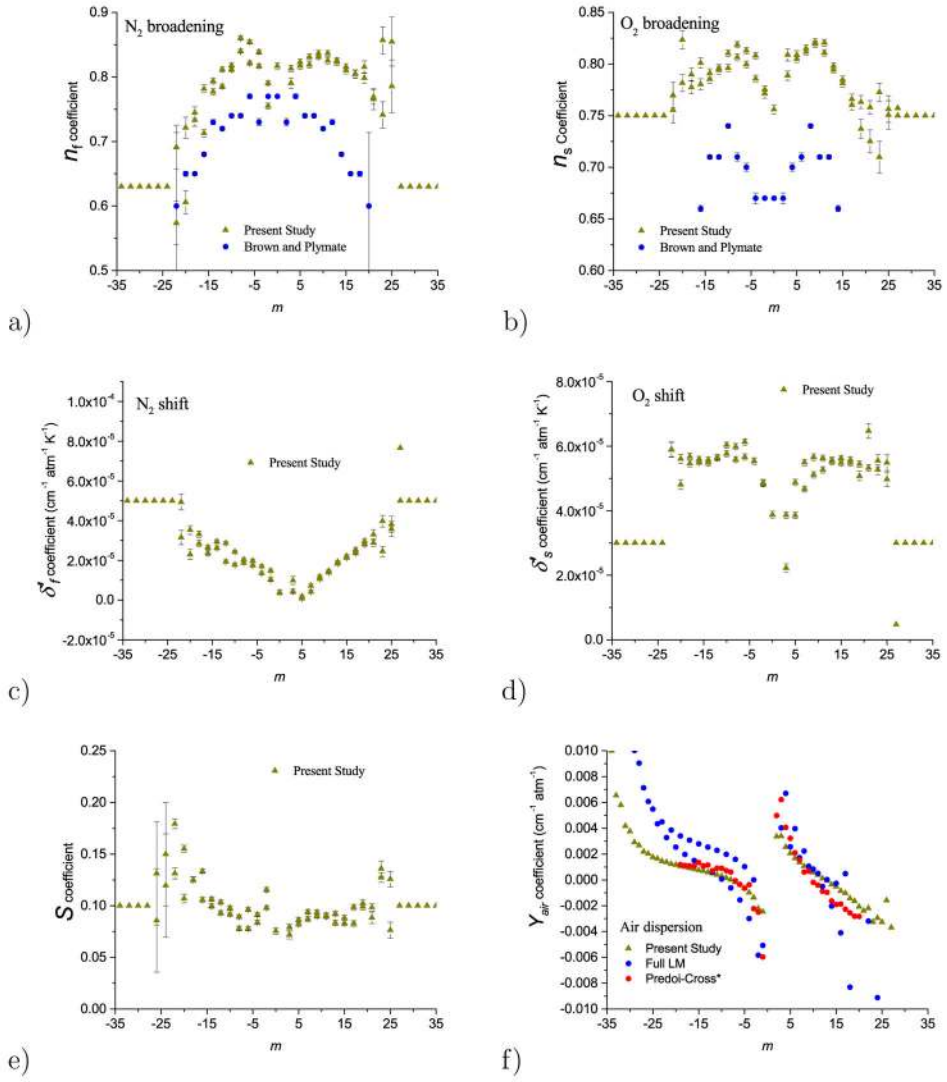

Figure 12.

Least squares fitted and fixed values in the LBL for oxygen A-band. (a) nitrogen broadening temperature exponents, this work [green], Brown and Plymate [21] [blue] (b) oxygen broadening temperature exponents [green], Brown and Plymate [21] [blue] (c) linear temperature dependences of the nitrogen pressure shift (d) linear temperature dependences of the oxygen pressure shift (e) speed dependence values (f) dispersion coefficients for air broadening compared with values obtained from Ref. [22] and calculated from data in Refs. [12, 13].

Table 1

Datasets and experimental conditions used for multispectrum fitting of the oxygen A-band. Errors (in parenthesis) on pressure, temperature are standard deviations of the measured values, and on pathlength and mixing ratio are from calibration data.

Method	Pres. (kPa)	Temp. (K)	Path (m)	X_{O_2}	OPD[c] (m)	cal[d] (x10[10])
CRDS	0.13112(4)[a]	295.28(12)	3,500.[b]	1.0000	–	0
CRDS	0.1320(1)[a]	296.31(15)	3,500.[b]	0.20720(43)	–	0
CRDS	53.37(2)	296.55(15)	3,500.[b]	0.20720(43)	–	0
CRDS	131.42(4)	294.65(11)	3,500.[b]	0.20720(43)	–	0
FTS	33.201(33)	297.2(2)	82.73(17)	0.20720(43)	0.4167	186
FTS	26.771(53)	296.9(2)	99.25(20)	0.20720(43)	0.6429	124
FTS	53.776(107)	297.2(2)	99.25(20)	0.20720(43)	0.4167	−188
FTS	40.126(80)	294.9(2)	99.25(20)	0.3250	0.4167	313
FTS	19.369(39)	295.8(2)	99.25(20)	0.1057	0.500	42
FTS	26.673(16)	297.1(1)	52.00(05)	1.000000(1)	0.375	−2426
FTS	67.113(13)	297.5(1)	52.00(05)	1.000000(1)	0.300	−1606
FTS	89.502(269)	202.9(14)	52.00(05)	0.20720(43)	0.1125	−2600
FTS	109.41(54)	242.6(14)	52.00(05)	0.20720(43)	0.150	−2600
FTS	111.26(45)	246.8(12)	52.00(05)	0.20720(43)	0.150	−2600
FTS	53.270(53)	209.0(7)	52.00(05)	0.20863(21)	0.225	−3000
FTS	133.38(13)	210.2(6)	52.00(05)	0.20863(21)	0.225	−3000
FTS	119.91(19)	187.9(4)	52.00(05)	0.20863(21)	0.225	−3000
FTS	56.417(56)	188.3(4)	52.00(05)	0.20863(21)	0.225	−3000
FTS	55.310(17)	204.9(6)	52.00(05)	1.000000(1)	0.225	−3000
FTS	105.86(21)	206.8(6)	52.00(05)	1.000000(1)	0.225	−3000
FTS	96.172(96)	188.7(5)	52.00(05)	1.000000(1)	0.225	−3000
FTS	133.28(13)	188.9(4)	52.00(05)	1.000000(1)	0.1286	−3000

[a] empirically adjusted value

[b] value at 13050 cm^{-1} based on cavity finesse

[c] Optical Path difference (OPD) is 1/(2 * *resolution*)

[d] Calibration factor, d_1 is defined in Eq. 2

Table 2

Least-squares fitted values for the O_2 A-band $^1\sum_g^+(v=0)$ Hamiltonian. All parameters are given in cm^{-1}.

Parameter	This study	Ref. [41]
$G_0(b^1\sum_g^+)$	13122.006033(8)	13122.005748(9)[a]
$B_0(b^1\sum_g^+)$	1.39124765(8)	1.3912493(5)
$D_0(b^1\sum_g^+) \times 10^6$	5.3631(2)	5.36839(8)
$H_0(b^1\sum_g^+) \times 10^{11}$	−0.87(2)	−4.5(f)
$B_0(X^3\sum_g^-)$	1.437676036(f)	1.437676036(16)
$\lambda_0(X^3\sum_g^-)$	1.984751424(f)	1.984751424(40)
$\gamma(X^3\sum_g^-) \times 10^3$	−8.42537576(f)	−8.42537576(290)

[a] hypothetical $N = 0$, $J = 1$ energy removed

Table 3

Intensity related values for the O_2 A-band intensity and $^3\sum_g^-(v=0)$ Hamiltonian.

Parameter	This study	Long *et al.* [14]/[60]	Shermaul *et al.* [61]
$G_{ev}(Qa) \times 10^{28}$ (cm^2)	1.1973(9)		1.217(1)[a]
$c_1 \times 10^4$	−2.658(f)	−2.658	5.0(5)
$c_2 \times 10^6$	3.36(f)	3.36	
$\Sigma I_k(296) \times 10^{22}$(cm)	2.2547(2)	2.242(7)	2.270(2)[b]
$\mu_{SO}(\beta_e)$	0.027430(4)	0.02736(3)[c]	0.0271[a]

[a] factor of 2 (or $\sqrt{2}$) from Hönl-London factor applied

[b] present Q gives $2.260(2) \times 10^{-22}$cm

[c] $3j$ normalization factor of $\sqrt{\frac{5}{32}}$ applied

Table 4

P-branch LBL parameters determined by the multispectrum fitting of the oxygen A-band. Units are cm^{-1} for σ_0 and E''; cm^{-1}/(molec cm^{-2}), natural abundance of $^{16}O_2$, 0.99530 is included for I; cm^{-1} $atm.^{-1}$ (0.29587215 MHz/Pa) for γ_f, γ_s, δ_f and δ_s; $\times 10^5$ $cm^{-1}atm^{-1}K^{-1}$ (0.29587215 MHz/Pa/K) for δ'_f and δ'_s; and n_f, n_s, and S are unitless. Intensity, width and shift are referenced to 296 K, values in parenthesis are one standard deviation of the fitted or constrained fitted value, no parenthesis indicates a fixed value was used in the analysis.

quanta		σ_0	I (296K)	E''	γ_f	n_f	γ_s	n_s	δ_f	δ'_f	δ_s	δ'_s	S
P1	P1	13118.04495(1)	3.083E-24	3.9611	0.05977(11)	0.817(5)	0.05894(11)	0.756(5)	−0.00430(9)	−3.9E-06(1)	0.00108 (9)	3.9E-05(1)	0.076(3)
P3	Q2	13114.10046(1)	3.910E-24	16.2529	0.05947(7)	0.755(4)	0.05683(10)	0.771(4)	−0.00624(8)	1.0E-05(1)	−0.00026 (8)	4.9E-05(1)	0.115(2)
P3	P3	13112.01615(1)	5.754E-24	18.3372	0.05669(4)	0.791(3)	0.05535(8)	0.775(4)	−0.00652(6)	1.5E-05(1)	−0.00025 (8)	4.8E-05(1)	0.098(2)
P5	Q4	13107.62872(1)	6.008E-24	42.2001	0.05379(3)	0.839(3)	0.05311(7)	0.786(4)	−0.00754(6)	1.4E-05(1)	−0.00082 (8)	5.5E-05(1)	0.084(2)
P5	P5	13105.61713(1)	7.616E-24	44.2117	0.05379(3)	0.817(3)	0.05251(6)	0.808(3)	−0.00762(6)	1.7E-05(1)	−0.00073 (8)	5.5E-05(1)	0.091(2)
P7	Q6	13100.82198(1)	7.150E-24	79.6070	0.05140(3)	0.854(3)	0.05087(6)	0.800(3)	−0.00785(6)	1.7E-05(1)	−0.00093 (8)	6.1E-05(1)	0.078(2)
P7	P7	13098.84847(1)	8.474E-24	81.5805	0.05193(3)	0.822(3)	0.05067(6)	0.813(3)	−0.00785(6)	2.0E-05(1)	−0.00095 (8)	5.7E-05(1)	0.096(2)
P9	Q8	13093.65603(1)	7.329E-24	128.4920	0.04975(3)	0.860(3)	0.04941(6)	0.807(3)	−0.00795(5)	1.9E-05(1)	−0.00104 (8)	6.0E-05(1)	0.078(2)
P9	P9	13091.71056(1)	8.360E-24	130.4375	0.05016(3)	0.840(3)	0.04926(6)	0.819(3)	−0.00795(5)	2.0E-05(1)	−0.00098 (8)	5.6E-05(1)	0.089(2)
P11	Q10	13086.12530(1)	6.728E-24	188.8531	0.04905(3)	0.812(3)	0.04820(6)	0.796(3)	−0.00831(5)	1.8E-05(1)	−0.00109 (8)	6.0E-05(1)	0.092(2)
P11	P11	13084.20355(1)	7.487E-24	190.7748	0.04877(2)	0.818(3)	0.04810(6)	0.810(3)	−0.00763(5)	2.4E-05(1)	−0.00108 (8)	5.8E-05(1)	0.098(2)
P13	Q12	13078.22769(1)	5.637E-24	260.6824	0.04734(3)	0.812(4)	0.04691(7)	0.794(4)	−0.00840(6)	1.9E-05(1)	−0.00143 (8)	5.6E-05(1)	0.093(2)
P13	P13	13076.32743(1)	6.166E-24	262.5827	0.04760(2)	0.785(4)	0.04691(6)	0.796(4)	−0.00770(5)	2.9E-05(1)	−0.00139 (8)	5.7E-05(1)	0.104(2)
P15	Q14	13069.96203(1)	4.357E-24	343.9694	0.04600(3)	0.777(5)	0.04571(8)	0.785(5)	−0.00850(6)	2.6E-05(1)	−0.00168 (8)	5.6E-05(1)	0.100(2)
P15	P15	13068.08195(1)	4.706E-24	345.8495	0.04578(3)	0.794(4)	0.04570(7)	0.791(4)	−0.00789(5)	2.9E-05(1)	−0.00185 (7)	5.5E-05(1)	0.106(2)
P17	Q16	13061.32742(1)	3.126E-24	438.7010	0.04414(3)	0.782(6)	0.04441(9)	0.780(5)	−0.00897(6)	2.4E-05(1)	−0.00199 (8)	5.5E-05(1)	0.106(2)
P17	P17	13059.46667(1)	3.343E-24	440.5618	0.04523(3)	0.713(6)	0.04455(9)	0.801(5)	−0.00884(6)	2.7E-05(1)	−0.00213 (8)	5.6E-05(1)	0.133(2)
P19	Q18	13052.32291(1)	2.091E-24	544.8622	0.04266(3)	0.733(9)	0.04325(10)	0.777(6)	−0.00923(6)	2.8E-05(2)	−0.00233 (8)	5.5E-05(1)	0.125(3)
P19	P19	13050.48093(1)	2.220E-24	546.7042	0.04262(3)	0.745(9)	0.04308(10)	0.790(6)	−0.00853(6)	3.3E-05(2)	−0.00253 (8)	5.7E-05(1)	0.125(3)
P21	Q20	13042.94749(1)	1.308E-24	662.4359	0.04094(4)	0.606(18)	0.04074(13)	0.823(9)	−0.01004(7)	2.3E-05(3)	−0.00296 (11)	4.8E-05(2)	0.107(4)
P21	P21	13041.12385(1)	1.380E-24	664.2595	0.04093(4)	0.721(16)	0.04214(12)	0.782(8)	−0.00902(6)	3.5E-05(2)	−0.00305 (10)	5.6E-05(1)	0.155(3)
P23	Q22	13033.19994(1)	7.673E-25	791.4031	0.03872(4)	0.691(34)	0.04031(16)	0.755(13)	−0.01011(6)	4.9E-05(4)	−0.00314 (13)	5.9E-05(2)	0.131(5)
P23	P23	13031.39436(1)	8.051E-25	793.2087	0.03936(4)	0.574(34)	0.04093(16)	0.770(12)	−0.01033(7)	3.1E-05(4)	−0.00328 (12)	5.9E-05(2)	0.179(5)
P25	Q24	13023.07889(1)	4.225E-25	931.7431	0.03681(5)	0.630	0.03871(17)	0.750	−0.01157(7)	5.0E-05	−0.00379 (17)	3.0E-05	0.119

quanta		σ_0	I (296K)	E''	γ_f	n_f	γ_s	n_s	δ_f	δ'_f	δ_s	δ'_s	S
P25	P25	13021.29112(1)	4.414E-25	933.5309	0.03656(5)	0.630	0.03906(17)	0.750	−0.01047(7)	5.0E-05	−0.00406 (17)	3.0E-05	0.150
P27	Q26	13012.58274(1)	2.187E-25	1083.4332	0.03552(8)	0.630	0.03649(29)	0.750	−0.01079(9)	5.0E-05	−0.00387 (29)	3.0E-05	0.086
P27	P27	13010.81262(1)	2.276E-25	1085.2033	0.03443(8)	0.630	0.03776(29)	0.750	−0.01117(9)	5.0E-05	−0.00455 (29)	3.0E-05	0.131
P29	Q28	13001.70969(1)	1.065E-25	1246.4486	0.03267(15)	0.630	0.03619(56)	0.750	−0.01174(15)	5.0E-05	−0.00383 (56)	3.0E-05	0.100
P29	P29	12999.95707(1)	1.106E-25	1248.2013	0.03251(14)	0.630	0.03565(53)	0.750	−0.01168(15)	5.0E-05	−0.00364 (54)	3.0E-05	0.100
P31	Q30	12990.45772(2)	4.889E-26	1420.7631	0.03223	0.630	0.03356	0.750	−0.01066	5.0E-05	−0.00660	3.0E-05	0.100
P31	P31	12988.72247(2)	5.059E-26	1422.4983	0.03153	0.630	0.03382	0.750	−0.01056	5.0E-05	−0.00735	3.0E-05	0.100
P33	Q32	12978.82454(3)	2.115E-26	1606.3482	0.02948	0.630	0.03260	0.750	−0.01058	5.0E-05	−0.00674	3.0E-05	0.100
P33	P33	12977.10657(3)	2.184E-26	1608.0662	0.02906	0.630	0.03262	0.750	−0.01078	5.0E-05	−0.00702	3.0E-05	0.100
P35	Q34	12966.80765(5)	8.631E-27	1803.1737	0.02670	0.630	0.03200	0.750	−0.00960	5.0E-05	−0.00600	3.0E-05	0.100
P35	P35	12965.10688(5)	8.892E-27	1804.8745	0.02670	0.630	0.03200	0.750	−0.00970	5.0E-05	−0.00600	3.0E-05	0.100
P37	Q36	12954.40429(10)	3.325E-27	2011.2077	0.02570	0.630	0.03000	0.750	−0.01000	5.0E-05	−0.00600	3.0E-05	0.100
P37	P37	12952.72065(10)	3.418E-27	2012.8914	0.02570	0.630	0.03000	0.750	−0.01000	5.0E-05	−0.00600	3.0E-05	0.100
P39	Q38	12941.61143(17)	1.209E-27	2230.4162	0.02460	0.630	0.02900	0.750	−0.01000	5.0E-05	−0.00600	3.0E-05	0.100
P39	P39	12939.94486(17)	1.241E-27	2232.0828	0.02460	0.630	0.02900	0.750	−0.01000	5.0E-05	−0.00600	3.0E-05	0.100
P41	Q40	12928.42578(27)	4.156E-28	2460.7634	0.02340	0.630	0.02900	0.750	−0.01000	5.0E-05	−0.00600	3.0E-05	0.100
P41	P41	12926.77623(27)	4.259E-28	2462.4130	0.02340	0.630	0.02900	0.750	−0.01000	5.0E-05	−0.00600	3.0E-05	0.100
P43	Q42	12914.84379(40)	1.350E-28	2702.2117	0.02280	0.630	0.02800	0.750	−0.01000	5.0E-05	−0.00600	3.0E-05	0.100
P43	P43	12913.21121(40)	1.382E-28	2703.8443	0.02280	0.630	0.02800	0.750	−0.01000	5.0E-05	−0.00600	3.0E-05	0.100
P45	Q44	12900.86161(59)	4.146E-29	2954.7217	0.02230	0.630	0.02700	0.750	−0.01000	5.0E-05	−0.00600	3.0E-05	0.100
P45	P45	12899.24596(59)	4.238E-29	2956.3374	0.02230	0.630	0.02700	0.750	−0.01000	5.0E-05	−0.00600	3.0E-05	0.100

Table 5

R-branch LBL parameters determined by the multispectrum fitting of the oxygen A-band. Units are cm^{-1} for σ_0 and E''; cm^{-1}/(molec cm^{-2}), natural abundance of $^{16}O_2$, 0.99530 is included for I; cm^{-1} $atm.^{-1}$ (0.29587215 MHz/Pa) for γ_f, γ_s, δ_f and δ_s; $\times 10^5$ $cm^{-1}atm^{-1}K^{-1}$ (0.29587215 MHz/Pa/K) for δ'_f and δ'_s; and n_f, n_s, and S are unitless. Intensity, width and shift are referenced to 296 K, values in parenthesis are one standard deviation of the fitted or constrained fitted value, no parenthesis indicates a fixed value was used in the analysis.

quanta		σ_0	I(296K)	E''	γ_f	n_f	γ_s	n_s	δ_f	δ'_f	δ_s	δ'_s	S
R1	R1	13126.39224(1)	1.540E-24	3.9611	0.06137(17)	0.790(8)	0.05945(14)	0.809(6)	−0.00328(14)	−9.9E-06(2)	0.00141 (12)	2.2E-05(1)	0.072(4)
R1	Q2	13128.26903(1)	3.587E-24	2.0843	0.05740(11)	0.813(5)	0.05694(10)	0.789(5)	−0.00466(8)	−4.4E-06(1)	0.00081 (9)	3.9E-05(1)	0.079(3)
R3	R3	13131.49166(1)	4.306E-24	18.3372	0.05480(10)	0.817(5)	0.05413(9)	0.809(4)	−0.00484(7)	−1.7E-06(1)	0.00103 (8)	3.9E-05(1)	0.082(3)
R3	Q4	13133.44123(1)	6.244E-24	16.3876	0.05412(8)	0.823(5)	0.05359(7)	0.805(3)	−0.00538(6)	−8.2E-07(1)	0.00093 (8)	4.9E-05(1)	0.086(2)
R5	R5	13136.21726(1)	6.325E-24	44.2117	0.05197(8)	0.819(5)	0.05131(7)	0.815(3)	−0.00585(6)	4.2E-06(1)	0.00032 (8)	4.7E-05(1)	0.087(2)
R5	Q6	13138.20500(1)	8.059E-24	42.2240	0.05168(8)	0.831(4)	0.05103(6)	0.812(3)	−0.00624(6)	7.2E-06(1)	0.00032 (8)	5.5E-05(1)	0.094(2)
R7	R7	13140.56756(1)	7.380E-24	81.5805	0.04997(8)	0.837(5)	0.04952(6)	0.821(3)	−0.00628(6)	1.1E-05(1)	0.00006 (8)	5.1E-05(1)	0.090(2)
R7	Q8	13142.58345(1)	8.847E-24	79.5646	0.04976(7)	0.831(4)	0.04922(6)	0.819(3)	−0.00658(6)	1.2E-05(1)	−0.00002 (8)	5.7E-05(1)	0.094(2)
R9	R9	13144.54087(1)	7.479E-24	130.4375	0.04848(7)	0.825(5)	0.04816(6)	0.821(3)	−0.00668(6)	1.5E-05(1)	−0.00023 (8)	5.3E-05(1)	0.091(2)
R9	Q10	13146.58063(1)	8.652E-24	128.3977	0.04821(7)	0.836(4)	0.04805(6)	0.811(3)	−0.00687(6)	1.4E-05(1)	−0.00013 (8)	5.6E-05(1)	0.090(2)
R11	R11	13148.13530(1)	6.814E-24	190.7748	0.04694(8)	0.823(5)	0.04715(6)	0.794(4)	−0.00704(6)	1.8E-05(1)	−0.00051 (8)	5.5E-05(1)	0.092(2)
R11	Q12	13150.19673(1)	7.702E-24	188.7134	0.04676(7)	0.825(5)	0.04700(6)	0.798(3)	−0.00721(6)	1.9E-05(1)	−0.00035 (8)	5.6E-05(1)	0.083(2)
R13	R13	13151.34876(1)	5.678E-24	262.5827	0.04543(8)	0.815(5)	0.04574(7)	0.785(4)	−0.00755(6)	2.2E-05(1)	−0.00088 (8)	5.5E-05(1)	0.088(2)
R13	Q14	13153.43057(1)	6.313E-24	260.5009	0.04524(8)	0.810(5)	0.04574(6)	0.781(4)	−0.00753(6)	2.1E-05(1)	−0.00074 (8)	5.6E-05(1)	0.083(2)
R15	R15	13154.17894(1)	4.369E-24	345.8495	0.04387(9)	0.804(6)	0.04471(8)	0.766(5)	−0.00797(7)	2.5E-05(1)	−0.00144 (8)	5.6E-05(1)	0.099(3)
R15	Q16	13156.28033(1)	4.799E-24	343.7481	0.04346(8)	0.805(6)	0.04475(8)	0.760(5)	−0.00796(7)	2.4E-05(1)	−0.00065 (8)	5.5E-05(1)	0.083(3)
R17	R17	13156.62333(1)	3.123E-24	440.5618	0.04208(10)	0.798(8)	0.04332(10)	0.763(6)	−0.00854(7)	2.8E-05(1)	−0.00182 (8)	5.4E-05(1)	0.099(3)
R17	Q18	13158.74374(1)	3.399E-24	438.4413	0.04158(12)	0.815(9)	0.04337(14)	0.737(9)	−0.00856(8)	2.9E-05(2)	−0.00154 (11)	5.1E-05(1)	0.102(4)
R19	R19	13158.67919(1)	2.083E-24	546.7042	0.03991(15)	0.766(16)	0.04185(15)	0.725(11)	−0.00874(11)	3.3E-05(3)	−0.00155 (13)	6.5E-05(2)	0.088(6)
R19	Q20	13160.81826(1)	2.250E-24	544.5651	0.04018(11)	0.769(11)	0.04185(11)	0.758(7)	−0.00909(9)	2.9E-05(2)	−0.00231 (9)	5.3E-05(1)	0.098(3)
R21	R21	13160.34357(1)	1.300E-24	664.2595	0.03873(16)	0.741(21)	0.04071(13)	0.773(9)	−0.00955(12)	2.5E-05(3)	−0.00306 (10)	5.3E-05(2)	0.127(5)
R21	Q22	13162.50103(1)	1.395E-24	662.1020	0.03799(31)	0.857(21)	0.04315(36)	0.710(15)	−0.00765(21)	4.0E-05(3)	−0.00176 (30)	5.5E-05(2)	0.136(7)
R23	R23	13161.61331(1)	7.603E-25	793.2087	0.03632(22)	0.785(41)	0.03921(18)	0.751(14)	−0.01009(17)	3.6E-05(4)	−0.00353 (14)	5.5E-05(2)	0.126(8)
R23	Q24	13163.78895(1)	8.122E-25	791.0331	0.03494(20)	0.855(38)	0.03861(16)	0.756(13)	−0.01001(16)	3.8E-05(4)	−0.00317 (13)	5.0E-05(2)	0.076(8)

quanta		σ_0	I(296K)	E''	γ_f	n_f	γ_s	n_s	δ_f	δ'_f	δ_s	δ'_s	S
R25	R25	13162.48501(1)	4.177E-25	933.5309	0.03008(77)	0.630	0.02976(63)	0.750	–0.01393(38)	5.0E-05	–0.00307 (95)	3.0E-05	0.100
R25	Q26	13164.67869(1)	4.443E-25	931.3372	0.03154(24)	0.630	0.03742(17)	0.757	–0.01015(21)	7.7E-05	–0.00408 (17)	4.7E-06	0.100
R27	R27	13162.95504(1)	2.158E-25	1085.2033	0.02919(49)	0.630	0.03544(34)	0.750	–0.01188(24)	5.0E-05	–0.00327 (34)	3.0E-05	0.100
R27	Q28	13165.16664(1)	2.287E-25	1082.9917	0.02909(35)	0.630	0.03635(32)	0.750	–0.00966(23)	5.0E-05	–0.00342 (31)	3.0E-05	0.100
R29	R29	13163.01953(2)	1.049E-25	1248.2013	0.02548(95)	0.630	0.03469(72)	0.750	–0.01333(28)	5.0E-05	–0.00112 (66)	3.0E-05	0.100
R29	Q30	13165.24897(2)	1.109E-25	1245.9718	0.03311(35)	0.630	0.03426(62)	0.750	–0.01038(29)	5.0E-05	–0.00265 (60)	3.0E-05	0.100
R31	R31	13162.67439(3)	4.806E-26	1422.4983	0.03049	0.630	0.03170	0.750	–0.02336	5.0E-05	–0.00703	3.0E-05	0.100
R31	Q32	13164.92159(3)	5.065E-26	1420.2511	0.0143 (14)	0.630	0.0341 (12)	0.750	–0.00905(68)	5.0E-05	–0.00081(119)	3.0E-05	0.100
R33	R33	13161.91524(5)	2.075E-26	1608.0662	0.03161	0.630	0.03380	0.750	–0.00741	5.0E-05	–0.00647	3.0E-05	0.100
R33	Q34	13164.18017(5)	2.182E-26	1605.8012	0.02599	0.630	0.03137	0.750	–0.01118	5.0E-05	–0.00671	3.0E-05	0.100
R35	R35	13160.73749(10)	8.455E-27	1804.8745	0.02570	0.630	0.03000	0.750	–0.01050	5.0E-05	–0.01000	3.0E-05	0.100
R35	Q36	13163.02011(10)	8.871E-27	1802.5919	0.02570	0.630	0.03000	0.750	–0.01000	5.0E-05	–0.01000	3.0E-05	0.100
R37	R37	13159.13627(17)	3.252E-27	2012.8914	0.02460	0.630	0.02900	0.750	–0.01050	5.0E-05	–0.01000	3.0E-05	0.100
R37	Q38	13161.43654(17)	3.405E-27	2010.5911	0.02460	0.630	0.02900	0.750	–0.01000	5.0E-05	–0.01000	3.0E-05	0.100
R39	R39	13157.10644(27)	1.181E-27	2232.0828	0.02340	0.630	0.02900	0.750	–0.01050	5.0E-05	–0.01000	3.0E-05	0.100
R39	Q40	13159.42434(27)	1.235E-27	2229.7649	0.02340	0.630	0.02900	0.750	–0.01000	5.0E-05	–0.01000	3.0E-05	0.100
R41	R41	13154.64257(40)	4.052E-28	2462.4130	0.02280	0.630	0.02800	0.750	–0.01050	5.0E-05	–0.01000	3.0E-05	0.100
R41	Q42	13156.97810(40)	4.230E-28	2460.0774	0.02280	0.630	0.02800	0.750	–0.01000	5.0E-05	–0.01000	3.0E-05	0.100
R43	R43	13151.73899(59)	1.314E-28	2703.8443	0.02230	0.630	0.02700	0.750	–0.01050	5.0E-05	–0.01000	3.0E-05	0.100
R43	Q44	13154.09213(59)	1.370E-28	2701.4912	0.02230	0.630	0.02700	0.750	–0.01000	5.0E-05	–0.01000	3.0E-05	0.100
R45	R45	13148.38969(84)	4.030E-29	2956.3374	0.02170	0.630	0.02700	0.750	–0.01050	5.0E-05	–0.01000	3.0E-05	0.100
R45	Q46	13150.76045(84)	4.197E-29	2953.9666	0.02170	0.630	0.02700	0.750	–0.01000	5.0E-05	–0.01000	3.0E-05	0.100